JOURNAL OF GEOPHYSICAL RESEARCH, VOL. 95, NO. B10, PAGES 15,623–15,641, SEPTEMBER 10, 1990

Decrepitation and Crack Healing of Fluid Inclusions in San Carlos Olivine

B. J. WANAMAKER

Lawrence Livermore Laboratory, Livermore, California

TENG-FONG WONG

Department of Earth and Space Sciences, State University of New York at Stony Brook

BRIAN EVANS

Department of Earth, Atmospheric, and Planetary Sciences, Massachusetts Institute of Technology, Cambridge

Fluid inclusions break, or decrepitate, when the fluid pressure exceeds the least principal lithostatic stress by a critical amount. After decrepitation, excess fluid pressure is relaxed, resulting in crack arrest; subsequently, crack healing may occur. Existing models of decrepitation do not adequately explain several experimentally observed phenomena. We developed a linear elastic fracture mechanics model to analyze new data on decrepitation and crack arrest in San Carlos olivine, compared the model with previous fluid inclusion investigations, and used it to interpret some natural decrepitation microstructures. The common experimental observation that smaller inclusions may sustain higher internal fluid pressures without decrepitating may be rationalized by assuming that flaws associated with the inclusion scale with the inclusion size. According to the model, the length of the crack formed by decrepitation depends on the lithostatic pressure at the initiation of cracking, the initial sizes of the flaw and the inclusion, and the critical stress intensity factor. Further experiments show that microcracks in San Carlos olivine heal within several days at 1280 to 1400°C; healing rates depend on the crack geometry, temperature, and chemistry of the buffering gas. The regression distance of the crack tip during healing can be related to time through a power law with exponent n=0.6. Chemical changes which become apparent after extremely long heat-treatments significantly affect the healing rates. Many of the inclusions in the San Carlos xenoliths stretched, decrepitated, and finally healed during uplift. The crack arrest model indicates that completely healed cracks had an initial fluid pressure of the order of 1 GPa. Using the crack arrest model and the healing kinetics, we estimate the ascent rate of these xenoliths to be between 0.001 and 0.1 m/s.

INTRODUCTION

The study of fluid inclusions in mantle xenoliths has provided important information on the chemical speciation, fugacity, and migration of fluid at depth in the earth [*Roedder*, 1965; *Green and Radcliffe*, 1975; *Murck et al.*, 1978]. Most xenoliths are peridotite, and many of the fluid inclusions are filled with CO_2 under pressure.

Such fluid inclusions are small; their diameter is rarely larger than 30 μm, and usually less than 5 μm [*Roedder*, 1965]. Many submicron inclusions can also be observed with an electron microscope. Intragranular bubbles coarser than 1 to 2 μm in diameter may be dispersed throughout the xenolith grains or may occur in groups along curved planes of healed fractures [*Green and Radcliffe*, 1975; *Simmons and Richter*, 1976]. Microcracking appears to have initiated at fluid inclusions, apparently due to decrepitation of these inclusions during uplift of the xenolith [*Roedder*, 1965; *Wanamaker and Evans*, 1985; *Hall and Bodnar*, 1989].

If the fluid pressure inside an inclusion is significantly higher than the lithostatic pressure, then the stress field in the solid has a high deviatoric component in the local region surrounding the fluid inclusion. Localized failure can occur in either a brittle or a plastic mode. The latter process results in appreciable "stretching" of the inclusion [*Lawler and Crawford*, 1983; *Bodnar and Bethke*, 1984]. The elastic stress concentration is alleviated by plastic deformation accompanied by a reduction in fluid pressure. In contrast, brittle failure can occur if the lithostatic pressure and temperature are relatively low or if the difference between the fluid pressure and the lithostatic pressure is large or changing rapidly. Tensile cracks propagate from the fluid inclusion in a radial direction [*Larson et al.*, 1973; *Bodnar and Bethke*, 1984; *Bodnar,et al.*, 1989].

All of the above processes can modify significantly the crack geometry and connectivity, which, in turn, strongly influence the elastic, rheological, and transport properties of rocks [*e.g. Walsh*, 1965; *Brace*, 1977; *Shankland et al.*, 1981]. Both decrepitation and stretching change the fluid inclusion volume. If the volume change is not properly accounted for, error may be introduced into the use of fluid inclusion homogenization temperature as a paleotemperature and paleopressure indicator [*Larson et al.*, 1973; *Bodnar and Bethke*, 1984].

Some preliminary results on crack healing in San Carlos olivine were presented in *Wanamaker and Evans* [1985]. Results on fluid inclusion stretching behavior are described in detail in a companion paper [*Wanamaker and Evans*, 1989]. In

Paper number 90JB00478.
0148-0227/90/90JB-00478$05.00

this paper, we focus on the fracture mechanics of fluid inclusion decrepitation and the kinetics of crack healing. A theoretical model is developed and compared with our experimental observations. On the basis of our study of naturally decrepitated and healed fluid inclusions in San Carlos olivine, we suggest an interpretation of the conditions of their formation.

THEORETICAL ANALYSIS OF FLUID INCLUSION DECREPITATION

A theoretical analysis of fluid inclusion decrepitation should consider several attributes of brittle fracture which are observed naturally and experimentally. First, the decrepitation pressure (internal fluid pressure necessary to cause fracture) increases as a function of confining pressure [*Poland*, 1982]. Second, the decrepitation pressure at a given confining pressure depends on inclusion size: large fluid inclusions tend to crack at lower fluid pressure [*Roedder*, 1984; *Binns and Bodnar*, 1986; *Ulrich and Bodnar*, 1988; *Bodnar et al.*, 1989]. Third, the extent of cracking is a function of the inclusion dimension: larger inclusions tend to propagate cracks to greater distance before crack arrest [this study]. Theoretical results of previous analyses using elasticity theory are in qualitative agreement with some aspects of the experimental data. However, simple elastic models cannot account for the second and third observations and, in fact, predict no size effect at all. We suggest below that size dependence of decrepitation is related to stress concentrations induced by flaws which scale with inclusion size. This fracture mechanics model highlights the role of such irregularities on the initiation, propagation and arrest of brittle cracking and is more successful in predicting the experimental observations.

Often fluid inclusions are quite irregular in shape, but even in fairly regular fluid inclusions, at least two types of defects can exist. First, there may be small indentations or cracks on an otherwise smooth inclusion surface. If such cracks were smaller than a micrometer in dimension, they might pass undetected by optical microscopy. Their small size notwithstanding, these defects are potential nucleation sites for further cracking. Second, there are sharp corners on the fluid inclusion surface at intersections between negative crystal forms. In the plastic regime, stress concentrations which arise at geometric irregularities are reduced by dislocation flow; in the brittle field, cracks may nucleate.

In our model, we assume a simple spherical geometry following previous work in ceramics science [*e.g. Evans et al.*, 1979; *Green*, 1980] and in geophysical modelling of igneous dike intrusions [*Sammis and Julian*, 1987]. The stress concentration due to a geometric irregularity on the inclusion surface is modelled as that due to an annular crack on a spherical void (Figure 1). In some other situations more complicated geometrical assumptions are necessary. For example, in their recent

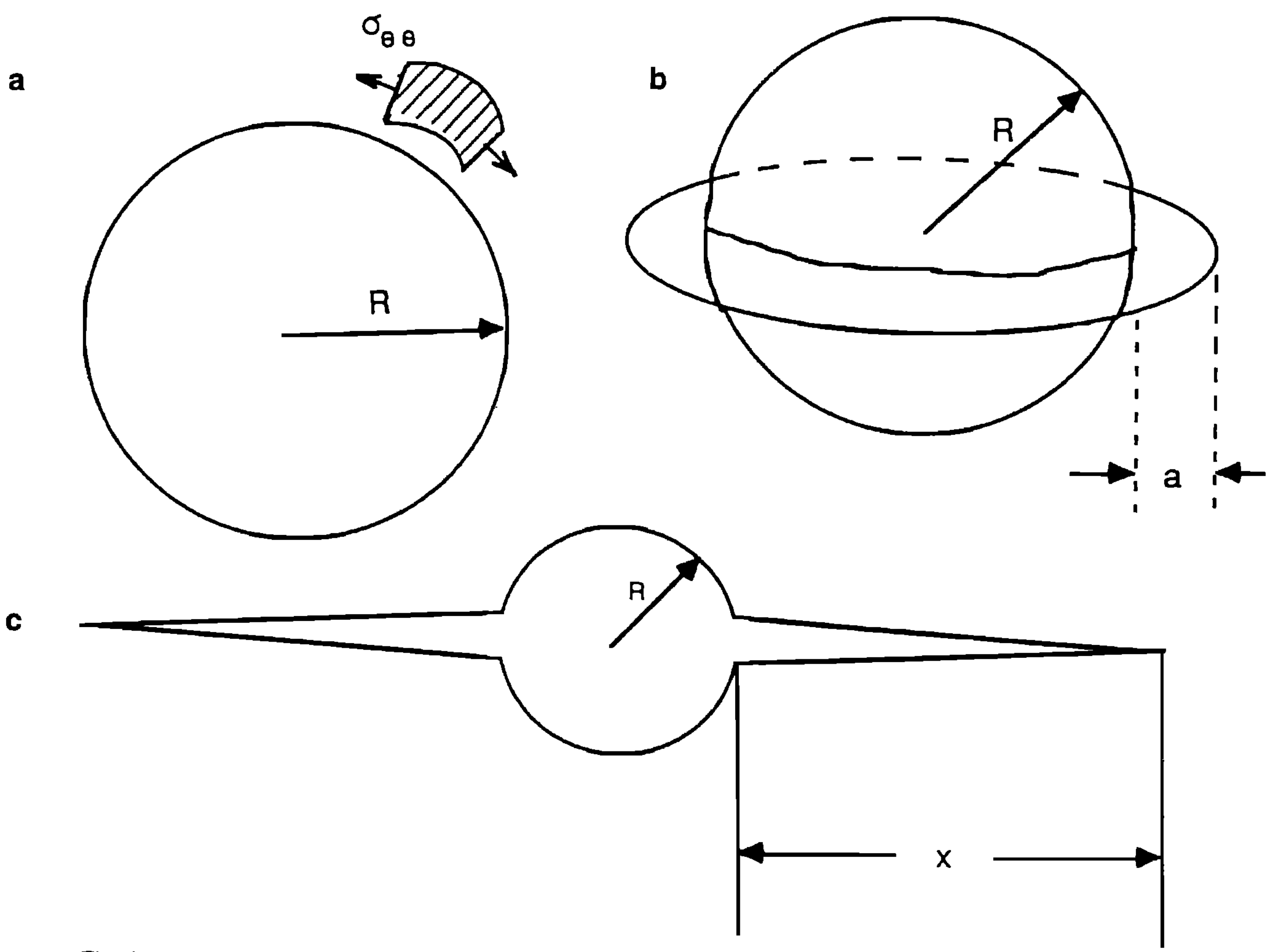

Fig. 1. (a) Orientation of the "hoop" stress in the neighborhood of a spherical fluid inclusion of radius R. If the "hoop" stress is sufficiently high, tensile cracking initiates in a radial direction. (b) An annular crack of length a at a spherical void of radius R. (c) Propagation of an annular crack to a final length X before crack arrest occurs.

analysis of thermal cracking, *Fredrich and Wong* [1986] concluded that a spherical inclusion model was not adequate to interpret grain boundary cracking. They developed a square inclusion model which reproduced all of the important features of the observed micromechanical processes. In contrast, our comparison with the observations of decrepitation shows that the spherical inclusion model outlined below captures most of the physics of decrepitation. Considering the limited observations, more detailed numerical treatment to include geometric complexity is probably not warranted at this stage. The fracture mechanics approach here is in the spirit of recent analyses of hydraulic fracturing [*e.g. Rummel and Winter*, 1983], igneous dike intrusions [*Sammis and Julian*, 1987], thermal cracking in rocks [*Fredrich and Wong*, 1986], and cracking induced by voids in ceramics [*e.g. Evans et al.*, 1979; *Green*, 1980], but these previous studies only considered crack initiation and did not attempt to consider the effect of pore pressure decrease on crack arrest.

Decrepitation Pressure: The Elasticity Solution

Although the geometry is somewhat different, the physical process for fluid inclusion decrepitation is analogous to that for hydraulic fracturing, the simplest theoretical analysis of which is based on elasticity theory. Decrepitation is assumed to initiate at the inclusion surface. For a spherical void in a linearly elastic medium, the maximum "hoop stress", $\sigma_{\theta\theta}$ (Figure 1a), attained at the spherical surface is given by

$$\sigma_{\theta\theta} = \frac{P_f}{2} - 3\frac{P_c}{2} \tag{1}$$

[*Timoshenko and Goodier*, 1951, p.395]. Here P_f is the fluid pressure inside the inclusion and P_c is the lithostatic pressure (or the confining pressure in the laboratory). Tension is taken to be positive. Decrepitation occurs if the "hoop stress" on the inclusion surface reaches the tensile strength of the solid, T. That is, the fluid pressure has to reach the decrepitation pressure given by

$$P_f^0 = 2T + 3P_c \tag{2}$$

Tugarinov and Naumov [1970] reported an increase of the decrepitation pressure with Mohs hardness in their room pressure study of fluid inclusions in ten minerals. Since hardness positively correlates with brittle strength [*Ohnaka*, 1973], *Tugarinov and Naumov's* [1970] data agree with the simple elasticity analysis. The decrepitation pressure in fluorite increases with confining pressure [*Poland*, 1982], also in qualitative agreement with the elasticity analysis (Figure 2a).

However, several experimental observations cannot be explained adequately using the simple elasticity solution. First, the data of *Bodnar et al.* [1989] on synthetic quartz (Figure 2b) show that relatively large fluid inclusions have low decrepitation pressures and vice versa. In contrast, the elasticity solution predicts a decrepitation pressure independent of inclusion size. Second, equation (2) predicts the ratio, P_f^0/P_c to be exactly equal to 3, whereas *Poland's* [1982] data fall on a slope which is less than 3 (Figure 2a). At elevated pressures, her data are consistently lower than those predicted by the elastic theory, even if we assume the tensile strength to be zero. Finally, the above model predicts a spherically symmetric stress field. Once the decrepitation pressure is reached, decrepitation can occur at any point on the spherical surface. In reality, decrepitation probably initiates at a particular location, at some lower pressure, owing to stress concentrations at a geometric irregularity.

The "hoop stress" in the vicinity of a spherical void of radius R subjected to an internal fluid pressure P_f is proportional to $(R/r)^3$ where r is the radial distance from the center of the void [*Timoshenko and Goodier*, 1951]. To explain the inverse correlation between decrepitation pressure and fluid inclusion size they observed in synthetic quartz, *Bodnar et al.* [1989] used the elasticity solution to argue that since the stress at a fixed distance r is proportional to R^3, a larger fluid inclusion induces a higher stress concentration and hence decrepitates at a lower pressure. However, this argument is incorrect since decrepitation is generally observed to initiate from the inclusion surface ($r=R$) which, according to the elasticity solution, has the maximum "hoop stress" value given by eq. (1), independent of the inclusion size. Once decrepitation has initiated, the stress field is perturbed by the inclusion-emanated crack and the elasticity solution is no longer valid for describing the stress field at a given radial distance r. Instead, a fracture mechanics solution should be employed.

Bodnar et al. [1989] also suggested that the size effect of decrepitation pressure is related to the size effect of the tensile strength of quartz: the larger the sample size, the lower the strength T, and hence, according to the elasticity solution in eq. (2), the lower the decrepitation pressure. However, it should be noted that the intrinsic tensile strength of quartz is independent of sample size. The apparent decrease of tensile strength with sample size is usually attributed to the higher probability of a larger sample to have a longer pre-existing microcrack. Again, a proper consideration of this problem requires the use of fracture mechanics.

Onset of Decrepitation

We consider the onset of growth of a crack emanating from the surface of a spherical void of radius R embedded in an elastic medium. The interior of the inclusion is subjected to fluid pressure, P_f, while a remote confining pressure, P_c, is applied to the solid. Despite the idealized geometry, this model provides useful insight into the dependence of decrepitation on the dimensions of the inclusion and preexisting defects. Geometric irregularities on the fluid inclusion surface are modelled by inserting an annular crack of length a (Figure 1b). Mathematical details are given in the Appendix.

For an initial flaw of length a, which is relatively short in comparison to the fluid inclusion radius R, the stress singularity near the crack tip can be approximated as that due to an edge crack of the same dimension in a semi-infinite medium [*Evans et al.*, 1979; *Green*, 1980]. As is elaborated in the Appendix, a reasonable estimate of the stress intensity factor in a tensile mode is

$$K_1 = 1.68(P_f - P_c)\sqrt{\pi a} \tag{3}$$

If either P_f increases or P_c decreases, the stress intensity factor increases. Once K_1 reaches a critical stress intensity factor (the fracture toughness K_{1c}), decrepitation occurs [*Lawn and Wilshaw*, 1975]. The fluid pressure at the onset of decrepitation, P_f^0 must satisfy the following relation

$$\boxed{P_f^0 - P_c = \frac{K_{1c}}{1.68\sqrt{\pi a}}} \tag{4}$$

The upper and lower bounds on decrepitation pressures for fluorite at elevated confining pressures obtained by *Poland* [1982] are compared with equations (2) and (4) in Figure 2a.

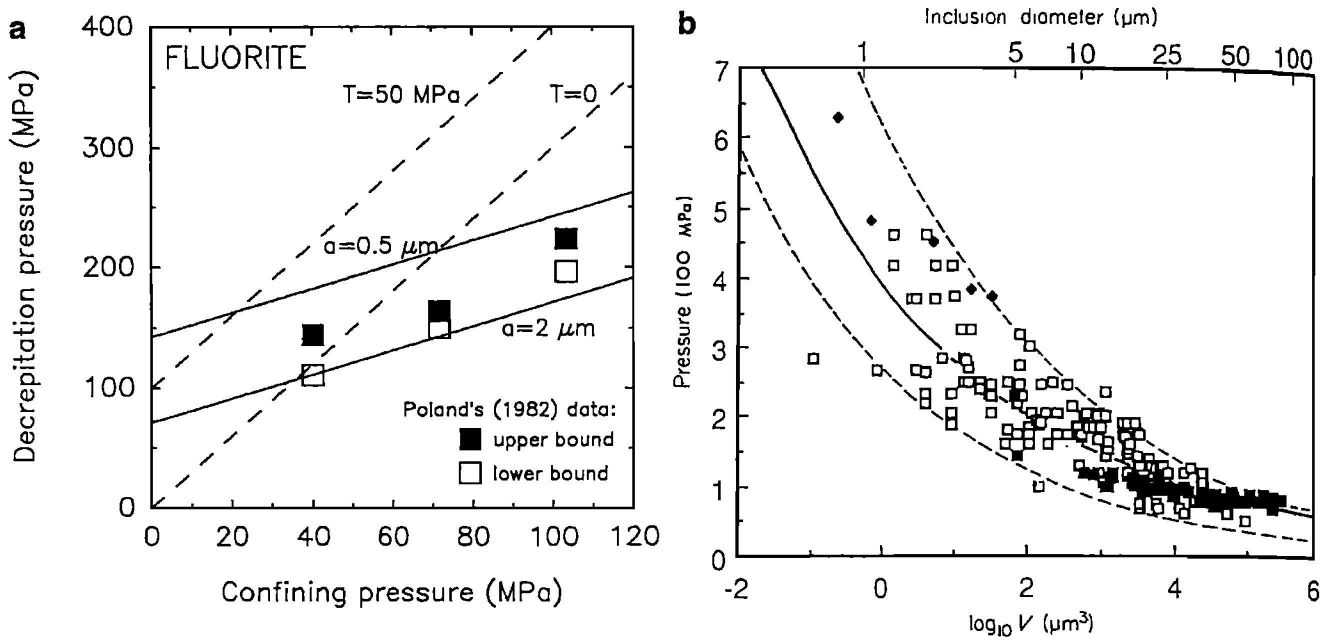

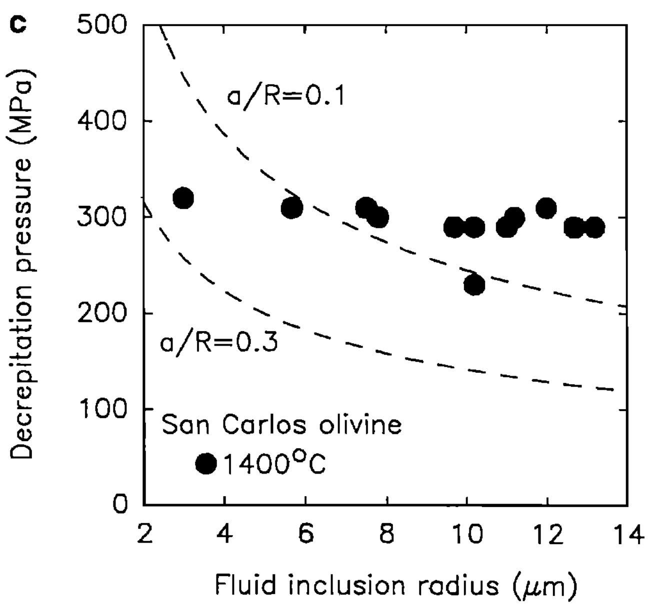

Fig. 2. (a) *Poland's* [1982] measurements of decrepitation pressure of fluorite as a function of confining pressure. Individual data points were bracketed by the upper and lower bounds shown. The dotted lines correspond to the elasticity solution (equation 2). The solid lines correspond to the fracture mechanics analysis (equation 4). (b) Decrepitation pressure of quartz synthetic inclusions as a function of fluid inclusion volume and diameter (assuming a spherical geometry). The data for a total of 191 fluid inclusions were compiled by *Bodnar et al.* [1989]. The solid line is the regression relation (eq. 5) determined by *Bodnar et al.* [1989]. The upper and lower dashed curves correspond to the fracture mechanics solution (eq. 4) for a/R equal to 0.08 and 0.42 respectively, where R is the fluid inclusion radius and a is the length of the initial flaw. (c) Upper bounds on decrepitation pressure of San Carlos olivine as a function of fluid inclusion radius. The dashed curves correspond to the fracture mechanics solution (equation 4).

Notice that the data at confining pressures of 72 and 103 MPa were all below the prediction of the simple elastic model. On the other hand, the theoretical curves corresponding to initial crack lengths of 0.5 μm and 2 μm bracket the experimental data reasonably well. K_{1c} was taken to be 0.30 MPa m$^{1/2}$ [*Gilman*, 1960].

Bodnar et al. [1989] presented preliminary data on decrepitation pressure for fluid inclusions in quartz and reported the following empirical relation between the fluid inclusion diameter D (in μm) and the decrepitation pressure P_f^0 (in kbars) at room pressure

$$P_f^0 = 4.26\, D^{(-0.423)} \tag{5}$$

These data are reproduced in Figure 2b, and the regression relation is shown by the solid curve. Assuming all the inclusions had a spherical geometry, we have plotted two dashed curves of the form $A/\sqrt{R}$ with A equal to 212 and 495 MPa μm$^{1/2}$, respectively. These two curves essentially bracket all the experimental data. There are limited data on fracture mechanics parameters of natural quartz, but extensive data are available for synthetic quartz [*Atkinson*, 1984], for which K_{1c} varies significantly with crack orientation. For comparison, if we take the highest value for K_{1c} reported by *Brace and Walsh* [1962], 0.41 MPa m$^{1/2}$, together with equation (3), then the two dashed curves in Figure 2b correspond to a/R=0.42 and 0.08, respectively. However, because the estimates are so sensitive to K_{1c} and since we do not have detailed information on the decrepitation orientation, the ratios a/R involve significant uncertainty. We have assumed a spherical geometry in the model, but the experiments involved fluid inclusions with shapes ranging from extremely irregular to spherical or negative crystal morphologies [*Bodnar et al.*, 1989]. This may explain why we need values of a/R differing by as much as a factor of 5 to bracket all the experimental data.

Arresting Phase of Decrepitation

Further progress using the fracture mechanics model requires us to calculate the evolution of the total pore volume and the fluid pressure as the crack extends. At the onset of cracking, a/R is relatively small, and the contribution of the crack to the total pore volume is negligible. Hence, the effective volume is given approximately by

$$V_0 = \frac{4}{3}\pi R^3 \tag{6}$$

As the crack extends, the total pore volume increases and the fluid pressure decreases. Suppose that the crack increases from the initial length, a, to a new value, X (Figure 1c). We show in the Appendix that if X is larger than the inclusion radius, R (as in these experiments), then the stress intensity factor can be evaluated using a Green's function technique and is given by the following analytic expression

$$K_1 = (2/\sqrt{\pi})(P_f - P_c) f(X/R)\sqrt{X} \tag{7}$$

where

$$f(X/R) = \frac{\sqrt{\frac{X}{R}+2}}{\sqrt{\frac{X}{R}+1}}\left[1+\frac{1}{2\left[\frac{X}{R}+1\right]^2}\right]$$

The stress intensity factor normalized by the crack length X is plotted in Figure 3a; K_1 normalized with respect to R is plotted in Figure 3b. The asymptotic value of K_1 for a very short crack (i.e., the initial propagation stage) is also shown in Figure 3a for comparison. Note that the stress intensity factor increases with the crack length, X, if the pressures are constant. Since fluid pressure variation is relatively small at first, initial crack propagation is probably unstable.

Once volume increases become appreciable, the stress intensity factor may drop below the critical value K_{1c} due to pore pressure reduction. This criterion is met when

$$P_f - P_c = \frac{\sqrt{\pi}K_{1c}}{2f(X/R)}\frac{1}{\sqrt{X}} \tag{8}$$

The fluid pressure is related to the effective inclusion volume through the equation of state of the fluid. The volume change can be calculated approximately by taking the total volume to be the sum of : (1) the spherical inclusion of volume V_0 and (2) a penny-shaped crack of radius $R+X$. Such an approach underestimates the opening at the juncture between the annular crack and the spherical surface. On the other hand, it probably overestimates the opening of the spherical surface.

Under the action of a fluid pressure P_f and confining pressure P_c, a penny-shaped crack of elliptical cross-section opens to attain an aspect ratio, α=maximum aperture/diameter, such that

$$\alpha = (4/\pi)(1-\upsilon^2)(P_f - P_c)/E \tag{9}$$

where E and υ are the Young's modulus and Poisson's ratio respectively [*Walsh*, 1965]. Since the semi-minor axis of the elliptical crack is $\alpha(X+R)$, the increase in volume is

$$\Delta V = (4\pi/3)\alpha(X+R)^3 \tag{10}$$

The fluid volumes and pressures at the initiation and arrest of the crack are interrelated through the equation of state. For a first approximation, if we assume that the perfect gas law describes the CO_2 in San Carlos olivine, then the following relation has to be satisfied

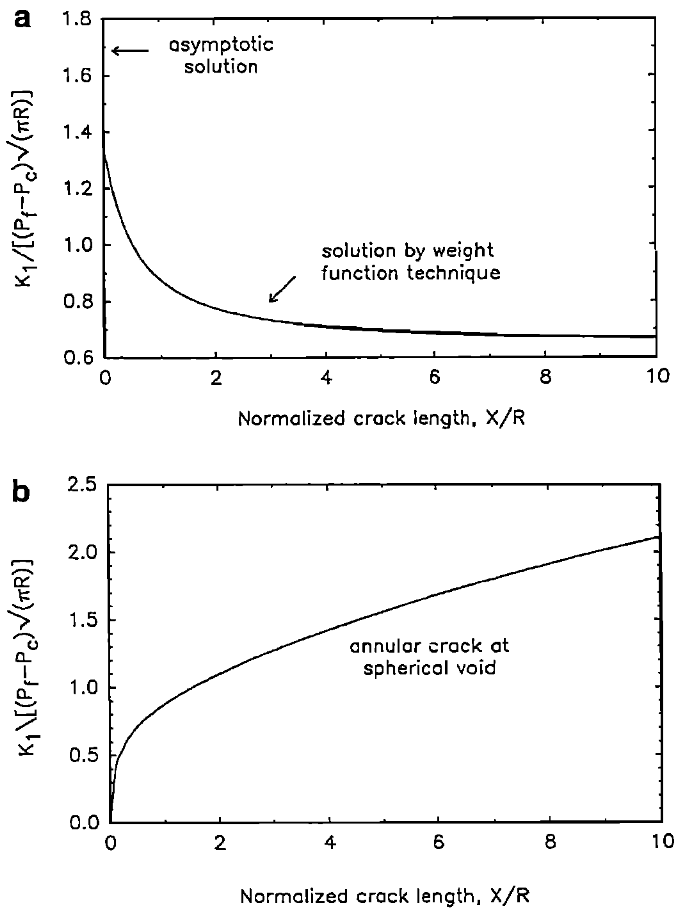

Fig. 3. (a) The stress intensity factor normalized with respect to the crack length X versus normalized crack length as given by equation (7). For comparison, the asymptotic value of the normalized stress intensity factor for a very short crack is also indicated. (b) The stress intensity factor normalized with respect to the fluid inclusion radius R versus normalized crack length as given by equation (7). Note that the stress intensity factor increases monotonically with crack length. This implies that crack propagation is unstable at a fixed pressure difference P_f - P_c, and crack arrest is possible only if P_f decreases or P_c increases.

$$(P_f^0 - P_f)/P_f = \Delta V/V_0 \tag{11}$$

Substituting equations (4) through (10) into equation (11), we arrive at an implicit equation relating the initial crack length a to the final crack length X

$$\frac{K_{1c}}{E\sqrt{R}} = f(\eta)\sqrt{\eta}\left[\frac{0.379f(\eta)\sqrt{(\eta/\beta)}-1}{1.128(1-\upsilon^2)(1+\eta)^3} - 1.128\frac{P_c}{E}\right] \tag{12}$$

with the non-dimensional parameters η=X/R and β=a/R. The crack extension (X) and its dependence on initial crack dimension, confining pressure, and fluid inclusion radius has been computed numerically and is shown in Figure 4a and 4b.

CRACK HEALING

Once a crack has been formed and propagates to arrest, surface tensions along the crack surface may result in transport of

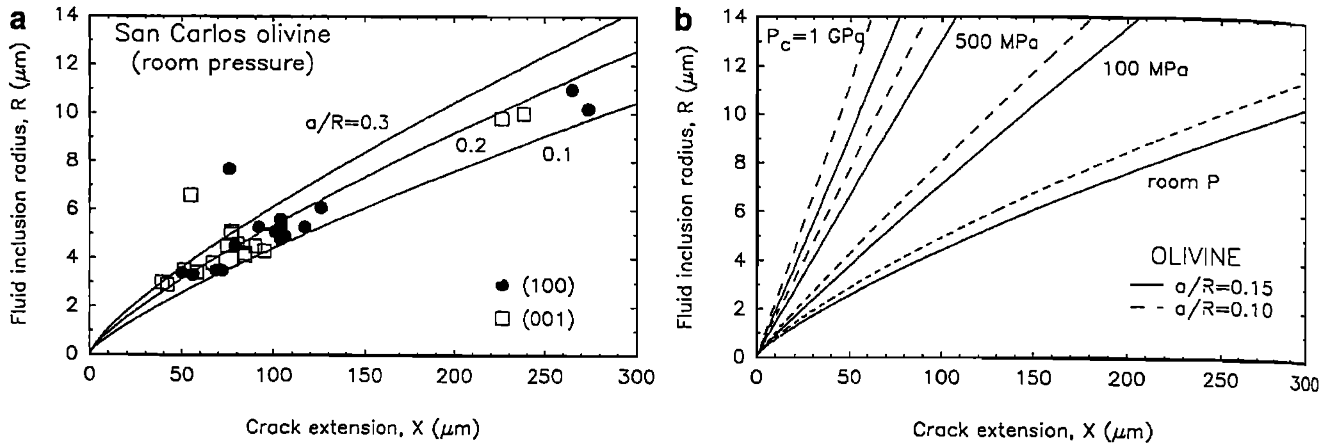

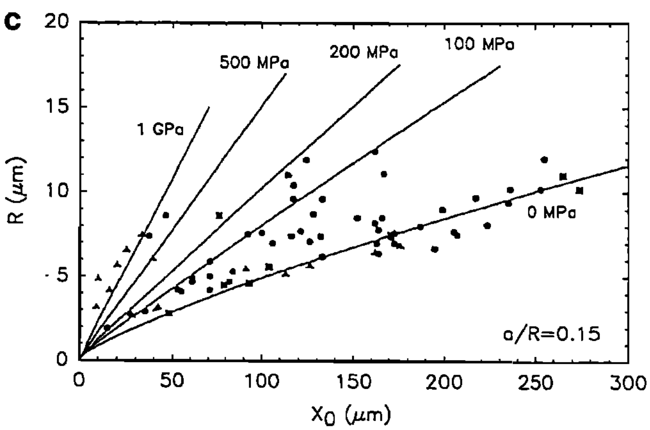

Fig. 4. (a) Relation between crack extension and fluid inclusion radius for decrepitation experiments on San Carlos olivine. The solid circles and open squares are data for cracks in the <100> and <001> directions, respectively. The continuous curves are theoretical results based on equation (12). (b) Theoretical curves based on equation (12) for confining pressures ranging up to 1 GPa. (c) Comparison of measurements of crack length as a function of fluid inclusion radius in natural and experimentally deformed samples with theoretical predictions based on equation (12). The triangles are completely healed natural cracks, circles are partially healed natural cracks, and squares are experimentally decrepitated cracks.

the solid by surface diffusion, lattice diffusion, evaporation-condensation, or solution-precipitation. Negatively curved surfaces, e.g. the crack tip, have lower chemical potentials than flat or positively curved surfaces and, hence, will act as sinks for the transported solid. If the source regions are located nearby on the surfaces of the crack, pore volume may be conserved during healing; however, pore shapes can be altered dramatically, as illustrated in Figure 5. For cracks which are connected to sources of material at chemical potentials higher than the local region around the crack tip, additional material may be transported into the cracked solid, i.e. crack sealing will occur. Workers studying fluid inclusions and cracks have observed many natural examples of crack healing and sealing (for example, see *Simmons and Richter* [1976], *Kirby and Green* [1980], and *Roedder* [1984]).

Transport of solid material to the crack tip results in the regression of the crack tip towards the open portion of the crack. The healing process sometimes involves a two-step process in which cylindrical tubes are first formed, followed by the formation of spherical pores, as shown schematically in Figure 5. This morphology is seen in the naturally healed cracks in San Carlos olivine. In other cases, the crack may heal by simply forming a single large pore [*Sprunt and Nur*, 1979; *Roedder*, 1984]. Laboratory experiments in brine-filled cracks in halite show that the transition between these two modes depends on the speed of the regression of the crack tip (S. H. Hickman and B. Evans, unpublished data, 1990).

Stability analyses by *Nichols and Mullins* [1965a, b] and numerical treatment by *Nichols* [1976] show that cylindrical tubes are unstable to perturbations in tube radius with wavelengths longer than a critical value determined by the method of transport. The instability results in the pinching off of spherical inclusions from the cylindrical pores, a process called ovulation. The analyses predict that the transport mechanisms may be identified by the ratio of spacing between the spherical inclusions to the radius of the cylinders. The time for ovulation, τ for a semi-infinite cylinder, in the case of transport via surface diffusion is

$$\tau = F(L/r_c) r_c^4 kT / D \gamma \Omega^2 N \tag{13}$$

where $F(L/r_c)$ is a function of the ratio of the length, L, of the cylinder to its radius, r_c, k is Boltzmann's constant, T is absolute temperature, D is the surface diffusion coefficient, γ is the surface energy of the material, Ω is the molecular volume, and N is the number of diffusing species per unit area.

Further progress in developing a rate law for crack healing involves specifying the transport mechanism, the crack shape, and the rate-limiting step in the evolution of pore shape. *Evans and Charles* [1977] developed a healing model assuming that the ovulation of spherical pores is the rate-limiting step in the crack healing process; that surface tension is isotropic; that the transport mechanism is surface diffusion; and that the width of the crack is given by a power law: $d_r = hu^j$ where d_r is the residual crack aperture, h is a function of crack length and previous loading geometry, u is the distance from the crack tip (see Figure 5), and the exponent j has a value between 0 and 0.5 (for the fully loaded condition). Because neither analytical nor numerical modeling of the formation of the cylindrical pores is available, assumptions regarding the rate of cylinder formation

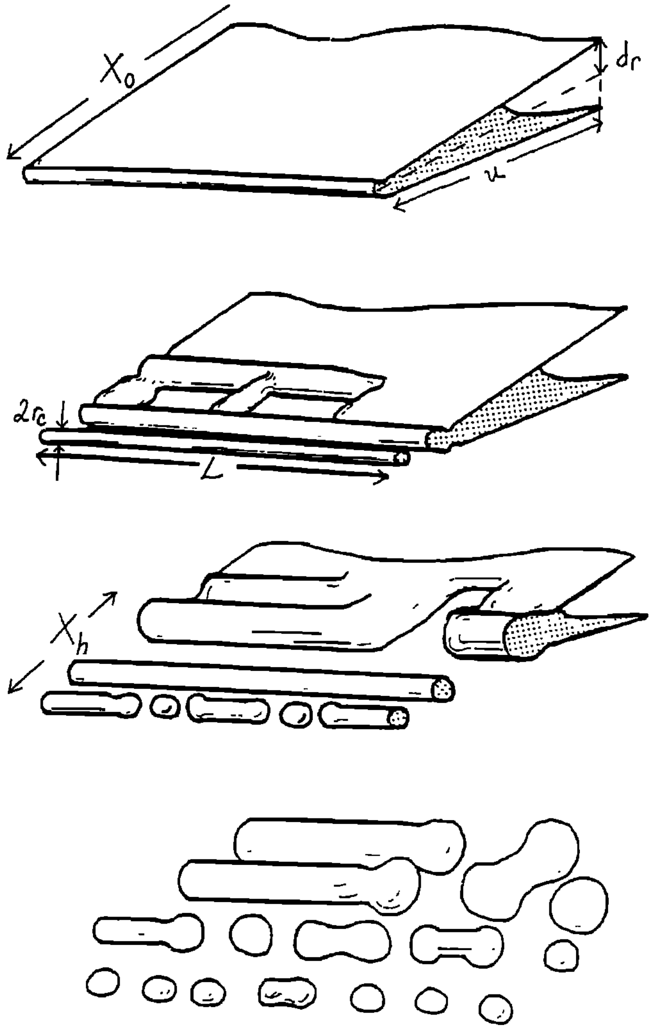

Fig. 5. Schematic diagram of changes in pore morphology during crack healing.

and the relationship of cylinder spacing to residual crack aperture are also necessary. Under these assumptions, the regression distance, X_0–X_h is related to time, t, by the following equation

$$\frac{X_0-X_h}{X_0} = A_m \left[\frac{C_m t}{kTX_0}\right]^n \tag{14}$$

where X_0 is the distance from the center of the crack to the original position of the crack tip, X_h is the distance to the present position of the crack tip, A_m is a dimensionless function ranging from 1.02 to 0.80 depending on the exact crack shape, and C_m is a function which depends on the shape factors mentioned above, the width of the crack at its center, and the surface diffusion coefficient.

The effect of geometry upon healing rate has been explicitly investigated for cracks in calcite filled with CO_2 at room pressure and temperatures between 780 and 850°C. *Hickman and Evans* [1987] added slight modifications to *Evans and Charles'* [1977] treatment to allow for cracks which were elliptical in cross section, rather than parabolic. For the early stage of crack healing, the kinetics are not strongly affected and the healing relation can be written

$$\frac{X_0-X_h}{X_0} = E_m \left[\frac{t e^{-Q/RT}}{T b_r^{\,w} X_0}\right]^n \tag{15}$$

where E_m depends on A_m and several other constants, Q is the activation energy for surface diffusion, R the gas constant, b_r the semi-minor axis of the ellipse, and w and n are constants which depend on assumptions regarding the geometry of cylinder formation [*see Hickman and Evans*, 1987]. Both of the models in eqs. (14) and (15) are based upon several assumptions and approximations, the most notable of which are the incorrect assumption of isotropic surface energy for olivine and the untested geometrical dependence of healing distance on the crack aperture. However, because the models have partial success in describing crack healing, we will use them as working models to place some constraints on the healing process. Assuming that $P_f = P_{lithostatic}$, the most important factors which may affect the rate of crack healing are temperature, crack size, and any chemical effects which may alter diffusion coefficients (e.g. in the case of olivine, changes in oxygen fugacity, or the introduction of melt).

EXPERIMENTAL PROCEDURE

We observed decrepitation of some inclusions in San Carlos olivine xenoliths during laboratory heat-treatments, providing data to compare with the fracture mechanics analysis; crack healing of both naturally decrepitated and experimentally decrepitated cracks in San Carlos olivine was also observed in the laboratory [*Wanamaker and Evans*, 1985]. Although some questions remain regarding healing kinetics, the previous experiments and a few additional ones place some constraints on the rates and mechanisms of healing.

Six different single crystals of San Carlos olivine were cut into plates parallel to either (010) or (100) which were roughly 1 cm x 1 cm x 1 mm; both sides were polished using alumina powders down to 0.3 μm. Diameters and fluid densities of several intact fluid inclusions in one or more sections from each crystal were measured using an optical microscope. Using a Chaix-Meca heating stage mounted on an optical microscope we measured the temperatures of melting and homogenization to a one-phase fluid; from these, compositions and fluid densities could be determined (see, for example, *Hollister and Crawford*, [1981]). The inclusions had a mean melting temperature of -56.6°C with a standard deviation of 0.2°C, consistent with pure CO_2 fluid. Homogenization temperatures were converted to fluid densities using the equation of state data for CO_2 of *Vukalovich and Altunin* [1969]. Inclusion diameter versus fluid density for the individual inclusions is plotted in Figure 6. The crack lengths, degree of crack healing, and inclusion diameters of naturally decrepitated fluid inclusions in the same crystal sections were also measured in directions parallel to <001> and <100> or <010> in transmitted light. For the naturally decrepitated inclusions, we assume that the present dimensions of the inclusion cavity, still clearly visible on the crack plane (Figure 7a), are the same as those of the inclusion prior to decrepitation. These parameters are listed in Table 1.

After measuring the dimensions and melting and homogenization temperatures of the enclosed fluid inclusions, one or more of the sections from each crystal were heated in a gas mixing furnace at 1280°C for 4 hours or at 1400°C for either 1 or 2.3 hours. Samples were heated and quenched at approximately 10°C/min. The furnace gas was maintained at a specific fO_2 between the iron-wustite and quartz-magnetite-fayalite buffers

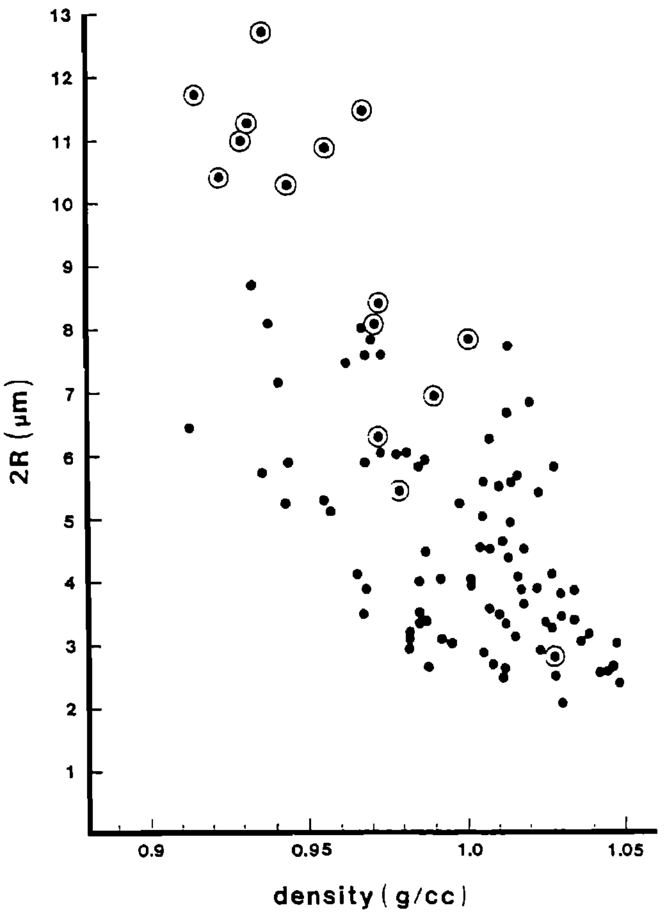

Fig. 6. Fluid density versus inclusion radius for fluid inclusions in the San Carlos olivine samples used in this study. Circled symbols are inclusions which decrepitated during the experiments.

by adding mixtures of either H_2 and CO_2 or CO_2 and CO. The experimental conditions for each crystal section are listed in Table 2. After the initial heat-treatment, some of the fluid inclusions contained in the crystal sections had decrepitated and formed "penny-shaped" cracks along (010) or (100) cleavage planes. Newly formed decrepitation cracks are optically visible due to the difference in refractive index between the CO_2-filled crack and the surrounding olivine and the characteristic pore morphologies accompanying incipient crack healing at the crack tip. Decrepitation is also corroborated by re-measuring the homogenization temperatures of the inclusions to verify a corresponding decrease in the fluid density. There are undoubtedly additional fluid inclusions which decrepitated in the samples but which were not included in this study. In particular, fluid inclusions less than approximately 5 μm in diameter were excluded because they were too small to accurately measure their melting and homogenization temperatures. The exclusion of these smallest inclusions may bias the results of this study. The sizes of the cracks were measured optically after quenching and are listed in Tables 3 and 4, along with the original fluid inclusion radii and, for the 1400°C experiments, fluid densities measured before heating. Unfortunately, none of the inclusions which decrepitated during the 1280°C heating had been measured using microthermometry, so their original fluid densities are unknown. In general, the cracks on (100) are longer in the

TABLE 1. Naturally Decrepitated Fluid Inclusions

Fluid Inclusion Radius R, μm		Crack Dimensions X_0, μm		Degree of Crack Healing $(X_0-X_h)/X_0$	
<100>	<001>	<100>	<001>	<100>	<001>
		SC201			
6.9	6.3	176	137	1.0	1.0
7.0	6.4	163	137	1.0	0.4
7.7	6.6	121	114	1.0	0.4
7.5	7.2	92	64		0.4
6.5	6.1	162	145	1.0	1.0
5.7	5.2	126	81	1.0	1.0
7.7	6.6	205	159	0.7	0.3
5.2	4.1	113	73	1.0	1.0
6.4	6.1	164	137	0.7	0.4
7.5	7.0	207	176	1.0	0.4
7.0	5.4	106	74	0.3	0.3
11.0	9.0	114	105	0.2	0.1
7.6	7.8	100	73	0.2	0.1
10.4	8.3	117	91	0.1	0.1
8.7	7.4	128	114	0.2	0.2
7.4	5.8	116	114	0.7	0.4
9.6	6.6	117	89	1.0	0.4
		SC702			
5.3	5.2	84	64		
4.2	3.9	71	45		
8.1	6.5	223	187	0.4	0.2
3.2	2.7	42	29	1.0	1.0
2.7	2.4	28	20	1.0	1.0
4.7	4.	81	61	1.0	1.0
2.8	1.7	27	21	1.0	1.0
5.9	4.4	71	42		
3.1	2.4	41	33	1.0	1.0
1.9	1.7	15	10		
7.4	5.1	132	102	0.3	0.3
8.2	8.3	162	129	0.3	0.3
6.7	6.8	195	154		
7.4	7.1	171	133	0.5	0.3
4.9	4.4	61	41		
8.5	7.1	152	124		
4.7	4.0	61	40		
8.0	10.0	187	181	0.3	0.2
4.7	4.5	82	72		
4.2	3.6	53	40		
5.0	4.6	71	48		
5.5	4.7	91	85	1.0	1.0
9.4	7.9	235	174		
		SC309			
11.9	11.8	124	104		
12.0	10.6	255	218	0.3	0.2
9.0	12.2	199	157		
		SC200			
9.6	8.1	133	109		
12.4	10.9	162	119		
		SC400			
7.1	5.8	126	100	0.0	0.0
10.2	7.7	236	162	0.0	0.0
7.6	8.4	173	128	0.0	0.0
8.5	7.2	166	123	0.0	0.0
10.2	7.9	253	263		
7.0	6.6	173	144	0.0	0.0
11.1	11.2	167	131	0.2	0.2
4.9	5.9	10	17	1.0	1.0
16.4	14.7	539	463	0.0	0.0
7.8	8.1	164	117	0.0	0.0
9.7	7.7	217	232	0.0	0.0
6.2	7.9	133	126	0.3	0.1
		SC601			
<010>	<001>	<010>	<001>	<010>	<001>
7.5	7.0	33	26	1.0	1.0
4.2	4.0	16	10	1.0	1.0
	2.9	44	35	0.0	0.0
5.7	5.2	20	20	1.0	1.0
3.2	2.9	9	9	1.0	1.0
6.6	5.2	25	30	1.0	1.0
7.4	7.1	37	31		
6.1	6.3	39	31	1.0	1.0
8.6	8.4	46	43		
4.1	3.6	55	65	0.0	0.0

TABLE 2. Experimental Conditions

Sample	Temperature, °C	Gas Mixture	fO_2, bars
601b	1400	H_2/CO_2	$10^{-10.0\pm0.1}$
701b	1400	H_2/CO_2	$10^{-10.0\pm0.1}$
103b	1400	H_2/CO_2	$10^{-6.5\pm1.0}$
103b*	1400	H_2/CO_2	$10^{-6.0\pm0.5}$
405d	1400	CO/CO_2	$10^{-10.2\pm0.2}$
602c	1400	CO/CO_2	$10^{-5.9\pm0.1}$
702c	1400	CO/CO_2	$10^{-5.9\pm0.1}$
405c	1400	CO/CO_2	$10^{-5.9\pm0.1}$
201	1280	H_2/CO_2	$10^{-10.2\pm0.5}$

*Last 72 hours.

TABLE 3. Fluid Inclusion Decrepitation at 1400°C

Crack	Fluid Inclusion Radius R, μm		Density, g/cm³	Crack Dimensions X_0, μm	
	<100>	<001>		<100>	<001>
702c-2	8.6	7.1	1.001	76	55
405d-10	10.2	10.0	0.734	274	238
701b-7	11.0	9.8	0.923	265	226
405c-1	5.6	5.0	0.955	104	77
702d-13	5.7	5.2	0.979	---	---
701a-2	2.8	2.7	1.028	48	42
103b-20	13.2	12.3	0.935	---	---
103b-22	10.2	12.4	0.932	---	---
103b-23	12.0	10.9	0.968	---	---
103b-25	7.5	6.4	0.988	171	126
103b-26	11.2	10.7	0.955	---	---
103b-27	7.8	12.8	0.942	---	---
	<010>	<001>		<010>	<001>
601b-4	9.7	12.3	0.930	---	---
601b-5	12.7	10.8	0.915	---	---
601b-18a	4.5	3.8	1.031	79	67
602c-D	4.6	4.4	---	93	81

TABLE 4. Fluid Inclusion Decrepitation at 1280°C

Crack	Fluid Inclusion Radius R, μm		Crack Dimensions X_0, μm	
	<100>	<001>	<100>	<001>
201-A	3.4	3.0	50	39
201-B	6.1	5.1	126	77
201-C	5.3	4.5	92	90
201-D	4.8	4.2	104	84
201-E	5.3	4.3	117	95
201-F	5.1	4.6	101	80
201-G	4.9	4.1	106	84
201-H	3.5	3.5	72	51
201-I	5.3	4.5	104	75
201-J	3.5	3.4	69	58
201-K	3.3	2.9	56	42

<001> direction than in the <010> direction. This asymmetry implies anisotropy in the fracture surface energies of olivine.

We selected some of the cracks which formed during the initial heating for subsequent crack healing experiments. The crystal sections containing these cracks were heat treated for periods of between 10 and 100 hours at the same temperature and fO_2 conditions as the initial heating. Figure 7 is a sequence of optical micrographs showing the progressive healing of crack 602c-D at 1400°C. After each experiment, the width of the healed region (X_h) of each crack was optically measured along either the <100> and <001> or <010> and <001> directions, starting at the original crack tip and ending at the edge of the unhealed region (see Table 5 and 6). The width X_h is shown schematically in Figure 5.

RESULTS OF DECREPITATION EXPERIMENTS

For our experiments on San Carlos olivine performed at 1400°C, we know the density of the fluid and therefore we can use the ideal gas law to calculate the maximum fluid pressure assuming no leakage. Of course, this value represents an upper bound on the decrepitation pressure since decrepitation could have occurred at any point during heating to 1400°C (Figure 2c). The theoretical curves were calculated based on eq. (4) assuming K_{1c} = 0.73 MPa m$^{1/2}$ for the (001) face. The value for the other cleavage surface (010) is somewhat lower (0.59 MPa m$^{1/2}$). As discussed above, we usually observed cracking on both planes. The pressure has to be above what we calculated before the onset of decrepitation on both cleavage surfaces occurs. Note that most of the experimental data fall above the curve for a/R = 0.1 and, taken together, the data suggest a range of values for a/R below 0.3, corresponding to an initial crack length on the order of a micrometer.

The physical parameters needed for our fracture mechanics model include the critical stress intensity factor and the elastic moduli. Following standard practice in this type of calculation for anisotropic crystals, we calculate an effective isotropic modulus for each specific orientation from the full elastic stiffness tensor as compiled in standard handbooks [*e.g. Simmons and Wang*, 1971]. Specifically, the elastic moduli for olivine (93% forsterite) are from *Kumazawa and Anderson* [1969] and critical stress intensity factor data for the (010) and (001) cleavage planes of olivine (88% forsterite) were obtained by *Swain and Atkinson* [1978].

All of our room pressure data on crack extension as a function of fluid inclusion dimension are plotted in Figure 4a. It can be seen from eq. (12) that if P_c = 0, then the physical parameters entering into the calculation are coupled as $(1-\upsilon^2)K_{1c}/E$. Since Young's moduli for the (010) and (001) faces are 167 GPa and 199 GPa respectively and Poisson's ratios are both 0.25, the values of $(1-\upsilon^2)K_{1c}/E$ for the two cleavage planes are both .003 $\sqrt{\mu m}$. Hence the theoretical curves shown in Figure 4 apply for both sets of cleavages.

In contrast to Figure 2c (in which the mean radius was used), in Figure 4a we show the data for the two cleavage planes separately. The projected dimension on the (100) plane tends to be longer and so is the crack extension. Except for one set of data, the experimental results are bracketed by the theoretical curves corresponding to values of a/R between 0.1 and 0.3. In this sense, the two sets of predictions (on decrepitation pressure and crack extension) of the fracture mechanics model are consistent with one another.

The numerical computations shown in Figure 4b illustrate the effect of confining pressure. In comparison with the experimentally decrepitated samples, the naturally decrepitated samples show a wider range of fluid inclusion dimension and crack extension (Figure 4c). Using eq. (12), the calculated lithostatic pressures experienced by San Carlos olivine during ascent range up to 1 GPa. This pressure is consistent with the petrologically estimated equilibration pressure of 900-2500 MPa [*Frey and Prinz*, 1978]. Such an elevated pressure will tend to inhibit crack extension and reduce the distance of propagation by as much as one half the value at room pressure. The computation was performed using parameters for the (010) face. For the (001) face, the corresponding values of lithostatic pressure can be obtained by multiplying the values in Figure 4c by a factor of 1.19.

a

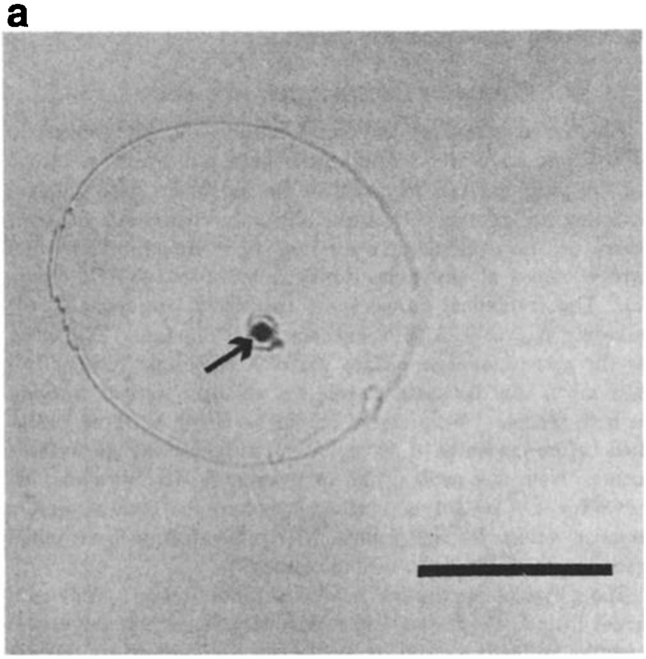

b

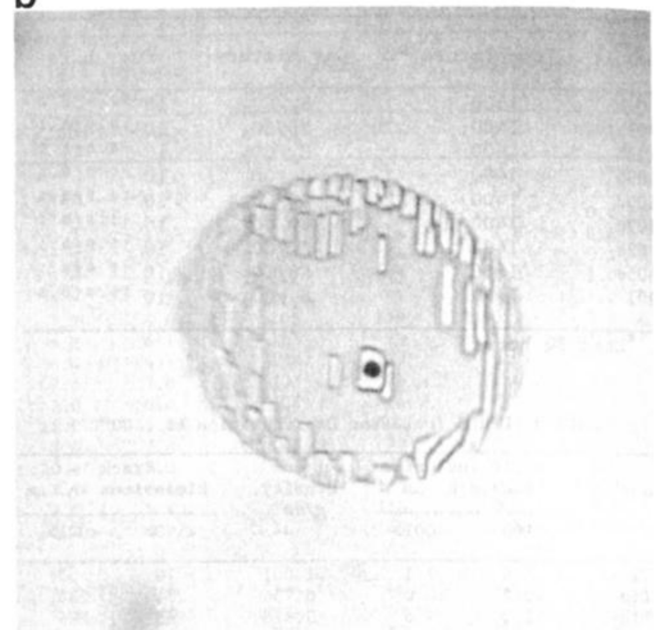

c

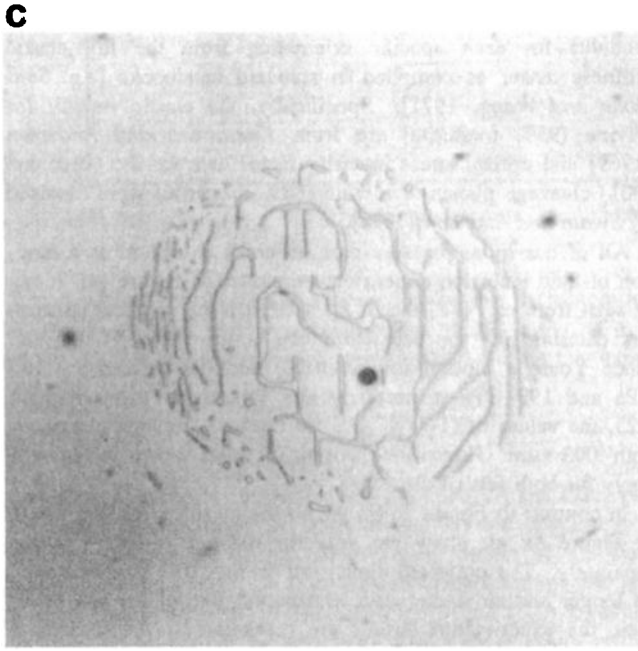

Fig. 7. Series of optical photomicrographs showing the progressive healing of crack 602c-D after: (a) 1 hour, (b) 11 hours, and (c) 111 hours at 1400°C. The scale bar is 100 μm. 'The original fluid inclusion is indicated by the arrow.

RESULTS OF CRACK HEALING EXPERIMENTS

The cylindrical pores formed during healing show a distinct crystallographic orientation, as shown in Figure 8. For experimentally healed cracks on both (010) and (100) (Figure 8a,b), the cylinder axis is parallel to <001>, whereas for naturally healed cracks on (010) (Figure 8c), the cylinder axis is parallel to <100>. If a partially healed, natural crack undergoes subsequent experimental healing, the orientation of the cylindrical pores changes accordingly, as shown in Figure 8e. The preferred orientation of the cylindrical pores may be a result of the shape anisotropy of the cracks, directional anisotropy of the surface energy, or directional anisotropy of diffusivity of olivine. Because the preferred orientation differs for experimentally and naturally healed cracks, the anisotropy may be a function of differing total pressure, temperature, oxygen fugacity, or crack width.

The approximate average length of the unhealed portion of the crack (X_0–X_h) is a decreasing function of time (Figure 9). The precision of the measurements are poor because distances are small and difficult to measure, the time steps are relatively coarse, the samples underwent subtle chemical changes which only became apparent after very long heat-treatments, and crack shape varies from crack to crack and from point to point within a given crack. For example, the aspect ratio of the cracks, as calculated by the ratio of r_c/X_0, varied from 0.002 to 0.009 and appeared to vary inversely with the crack area. In some cases the central portion of the crack near the original inclusion appeared to be narrower than some more distal points.

Healing rate is affected by temperature, crack width, and possibly oxygen fugacity. Cracks on the order of 2-30x10^3 μm^2 and approximately 1 μm thick are completely healed within 10-100 hours at 1400°C. There was no obvious difference in the rate of crack healing for cracks on different crystallographic planes. Not enough data are available to test the detailed relationship between X_0–X_h and time. However, if the two parameters are related by a power law (such as in eq. 15), the experimentally determined values of n range from 0.2 to 0.9, with a mean value of 0.6 and a standard deviation of ±0.3.

The data suggest a qualitative relationship between the width of the crack (as determined by the radius of the last formed cylinder) and the rate of crack healing (Tables 5 and 6; Figure 10), but considerable scatter is evident in the data. Following eq. 15 as a working model, the parameter w can be determined by plotting $\ln[(X_o-X_h)/X_0][X_0/t]^n T^n$ versus $\ln r_c^0$. Although precision is low, the best fit line indicates $w \approx 1.7$.

The mean of normalized crack length, $[(X_0-X_h)/X_0][X_o/t]^n T^n$, at 1400°C is 0.6, with values ranging from 0.07 to 2.4; the mean at 1280°C is 0.1, with values ranging from 0.09 to 0.16. Using the value of n = 0.6, and equa-

TABLE 5. Crack Healing Data at 1400°C

Crack	Average Crack Length X_0, μm <100>	$r_c^0 = b_r$[a], μm	Crack Shape Exponent j[a]	$(X_0-X_h)/X_0$		r_c^{Xh}, μm		Time, hours	Slope n[b]		Intercept A[b]		$\left[\frac{X_0-X_h}{X_0}\right]\left[\frac{X_0}{t}\right]^{n}T^{n}$
				<100>	<001>	<100>	<001>		<100>	<001>	<100>	<001>	
701b-G	28	0.25(±0.01)	0.03(±0.05)	0.175	0.14	0.15	0.25	1	0.74	0.82	-3.4	-3.8	0.81
				1.0	1.0	0.32		11					1.1
701b-7	265	0.54(±0.04)	0.38(±0.07)	0.035	0.07	0.15		1	0.46	0.25	-3.1	-2.1	0.63
				0.12	0.095	0.22	0.215	11					0.51
				0.30	0.225	0.35	0.325	111					0.32
701b-H	93	0.47(±0.04)	0.37(±0.06)	0.09	0.03	0.20		1	0.51	0.74	-3.0	-4.2	0.86
				0.135	0.165	0.23	0.225	11					0.31
				1.0	1.0	0.48	0.46	111					0.57
103b-25	171	1.07(±0.12)	0.37(±0.08)	0.03		0.27		2.33	0.69		-4.3		0.25
				0.16		0.53		65.33					0.18
				0.43		0.64		161.33					0.28
				1.0		1.05		233.33					0.52
405d-10	274	0.89(±0.77)	0.35(±0.26)	0.04	0.06	0.30	0.30	11	0.21	0.15	-2.4	-1.9	0.17
				0.065	0.085	0.415	0.43	109					0.07
702c-2	76	0.64(±0.06)	0.16(±0.05)	1.0	1.0	0.72	0.57	111					0.50
405c-1	104	0.62(±0.03)	0.21(±0.03)	1.0	1.0	0.63	0.56	11					2.40
	<010>			<010>	<001>	<010>	<001>		<010>	<001>	<010>	<001>	
601b-18a	79	0.33(±0.02)	0.04(±0.06)	0.065	0.06	0.275	0.28	1	0.90	0.25	-4.4	-2.1	0.56
				0.565	0.11	0.365	0.29	11					1.16
602c-D	93	0.65(±0.01)	0.16(±0.02)	0.27	0.205	0.525	0.54	11	0.57	0.69	-3.2	-3.8	0.61
				1.0	1.0	0.62	0.62	111					0.57
												mean	0.619 (±0.511)

[a]Determined from the fit to the equation: $r_c = r_c^0 (X_0 - X)^j$
[b]Determined from the fit to the equation: $(X_0 - X_h)/X_0 = At^n$

TABLE 6. Crack Healing Data at 1280°C

Crack	Average Crack Length X_0, μm	$(X_0-X_h)/X_0$		r_c^{Xh}, μm		Time hours	$\left[\frac{X_0-X_h}{X_0}\right]\left[\frac{X_0}{t}\right]^n T^n$
	<100>	<100>	<001>	<100>	<001>		
201-A	50	0.38	0.21	0.39	0.42	101	0.15
201-B	126	0.23	0.075	0.455	0.41	101	0.16
201-C	92	0.195	0.105	0.385	0.39	101	0.11
201-D	104	0.15	0.045	0.44	0.34	101	0.09
201-E	117	0.195	0.045	0.425	0.44	101	0.13
201-F	101	0.18	0.095	0.415	0.435	101	0.11
201-G	106	0.155	0.045	0.41	0.42	101	0.10
201-H	72	0.295	0.305	0.465	0.44	101	0.14
201-I	104	0.22	0.15	0.45	0.46	101	0.13
201-J	69	0.23	0.40	0.435	0.40	101	0.11
201-K	56	0.33	0.11	0.41	0.40	101	0.14
						mean	0.124 (±0.022)

tion 15, but *not* correcting for variations in crack width, the apparent activation energy, nQ/R, is roughly 29(±18)x10^3 K, where R is the gas constant in units of energy/mole. The accuracy of this determination is very difficult to calculate since it rests on several untested assumptions, an unverified model, and imprecise data; it is probably accurate to an order of magnitude only.

There are small, but systematic differences in crack healing rates when the oxygen fugacity is increased from 0.001 Pa to 0.1 Pa (10^{-8} to 10^{-6} bars). The time for ovulation of a cylinder of given radius seems to be longer for higher oxygen fugacity. Further, the ratio of the distance between spherical pores and the radius of the parent cylinder is 15.9±3.6 as compared with 7.8±1.9 at the lower fugacity. These observations are consistent with a change in mechanism from surface diffusion at 0.001 Pa fO_2 to lattice diffusion at 0.1 Pa fO_2. However, more evidence is needed to verify this hypothesis.

DISCUSSION

Fracture Mechanics of Fluid Inclusion Decrepitation

The above analysis is a rigorous fracture mechanics model for fluid inclusion decrepitation. The formulation of our model was motivated by recent experimental measurements of the decrepitation pressure as a function of confining pressure and fluid inclusion dimension. It is encouraging that the model predictions are in reasonable agreement with the experimental data of three minerals (fluorite, olivine, and quartz) that have significantly different mechanical properties.

Our fracture mechanics model has two key features. First, we postulate that the dimension of a pre-existing flaw scales with the fluid inclusion size. This is a plausible assumption since the nucleation of a pre-existing flaw has to be due to stress concentration in the local vicinity of the fluid inclusion, and the spatial distribution of such a stress perturbation has to scale with the inclusion dimension, the only characteristic length scale in the model. However, the physical mechanism which induces the local stress field is not well known. It is probably related to processes for the incorporation of the xenolith into the host magma and for the formation of the fluid inclusion [*Green and Radcliffe*, 1975; *Kirby and Green*, 1980; *Wanamaker and Evans*, 1985].

Second, we consider all three stages of the decrepitation process: initiation, propagation, and arrest. Therefore, our analysis is somewhat more involved than previous theoretical treatments of related geophysics [e.g. *Rummel and Winter*, 1983; *Fredrich and Wong*, 1986; *Sammis and Julian*, 1987] and materials science [e.g. *Evans et al.*, 1979; *Green*, 1980] problems. To analyze the crack arrest process, we have to consider the equation of state of the fluid phase. Our experimental results on the crack lengths in San Carlos olivine as a function of fluid inclusion radius (Figure 4a) can be explained by our fracture mechanics model. We are not aware of similar measurements on other minerals. It is hoped that more extensive data will be provided by future fluid inclusion studies to check the validity of our model. For mathematical convenience, we only performed the computations using the perfect gas law. It should be noted that the above analysis can be generalized to consider more complicated equations of state.

Since decrepitation may occur over a wide range of temperatures, pressures, and possibly time scales, and because the geometry of the inclusion can range from relatively smooth to highly irregular, it is therefore unrealistic to expect any micromechanical model to characterize quantitatively all aspects of the decrepitation process. Below we discuss some of the limiting assumptions.

Although the fracture mechanics model assumes quasi-static crack propagation, the cracking is expected to be unstable initially, and thus, the driving force is in excess of the energy dissipation ahead of the crack tip. Before being arrested, the crack will tend to "overshoot" to a distance longer than that predicted by our quasi-static analysis. Our estimate of crack extension X_0 is therefore a lower bound. Using the asymptotic value of K_1 for a very short annular crack to evaluate the decrepitation pressure also underestimates the decrepitation pressure. In addition we assume the effective volume change to be solely due to a penny-shaped crack. To resolve the fine details of volume change as a function of crack length, one would have to resort to a finite-element calculation using a very fine mesh.

The effects of pressure and temperature on the elastic moduli have been studied extensively in mineral physics. However, the dependence of K_{1c} on pressure and temperature is not as well known. The most significant effects will result from plastic processes operating near the crack tip in the semi-brittle regime. The effective fracture toughness increases due to inelastic dissipation induced by dislocation activity. In the brittle regime, the effect of pressure and temperature on K_{1c} of minerals is probably of second order. In the absence of reliable data on such

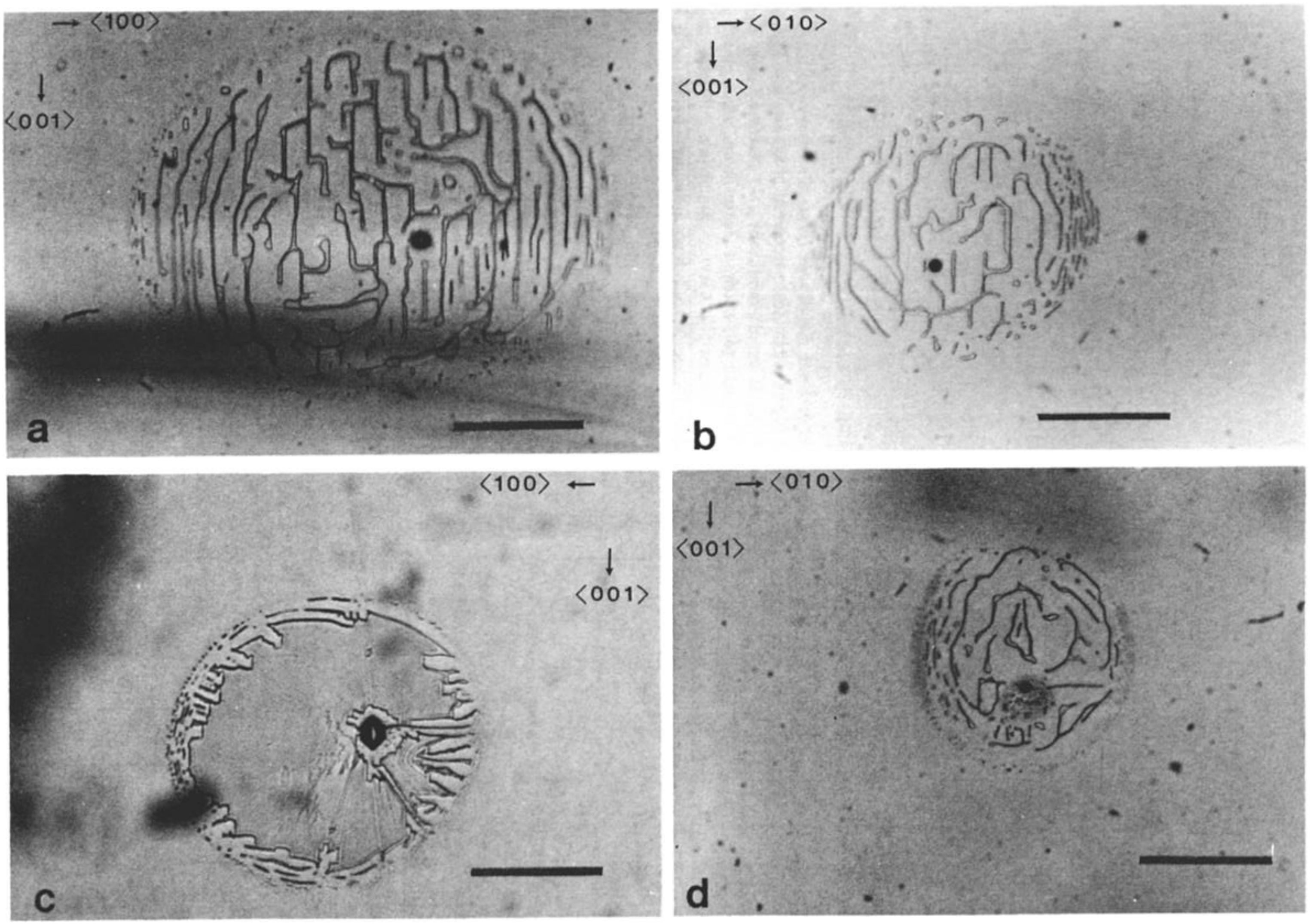

Fig. 8. Optical photomicrographs showing that the orientation of cylindrical pores is primarily parallel to <001> on (a) (010) and (b) (100), during experimental crack healing but parallel to (c) <100> on (010) and (d) <001> on (100) during natural crack healing. Changes in orientation of cylindrical pores are produced on a single crack (c) undergoing first natural and than experimental crack healing. Scale bars are 100 μm.

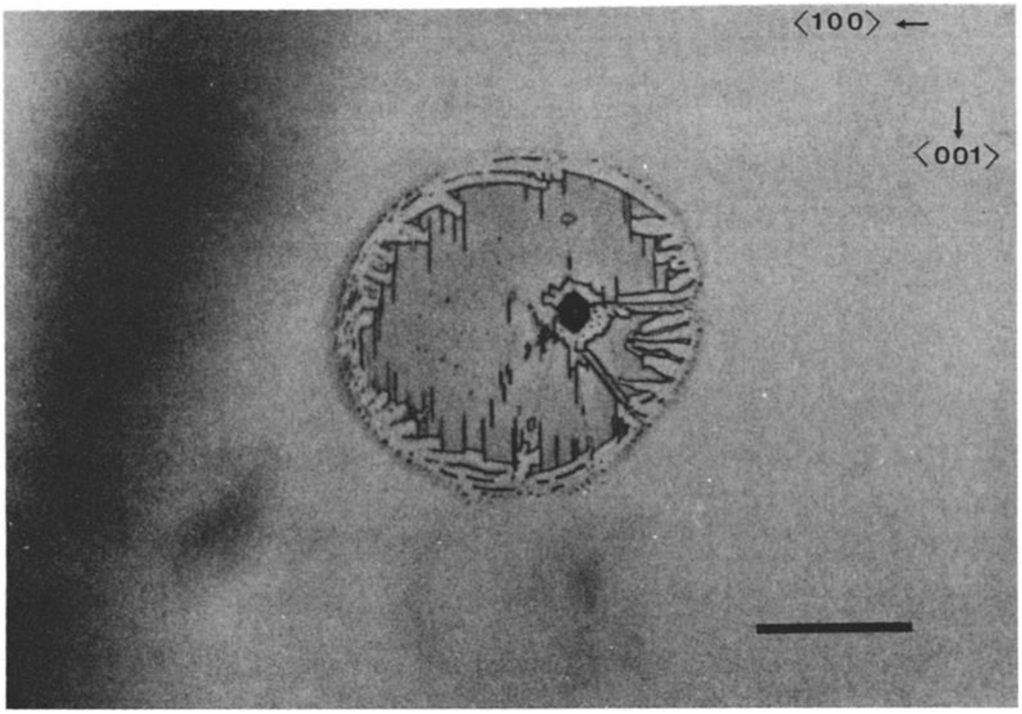

Fig. 8. (continued)

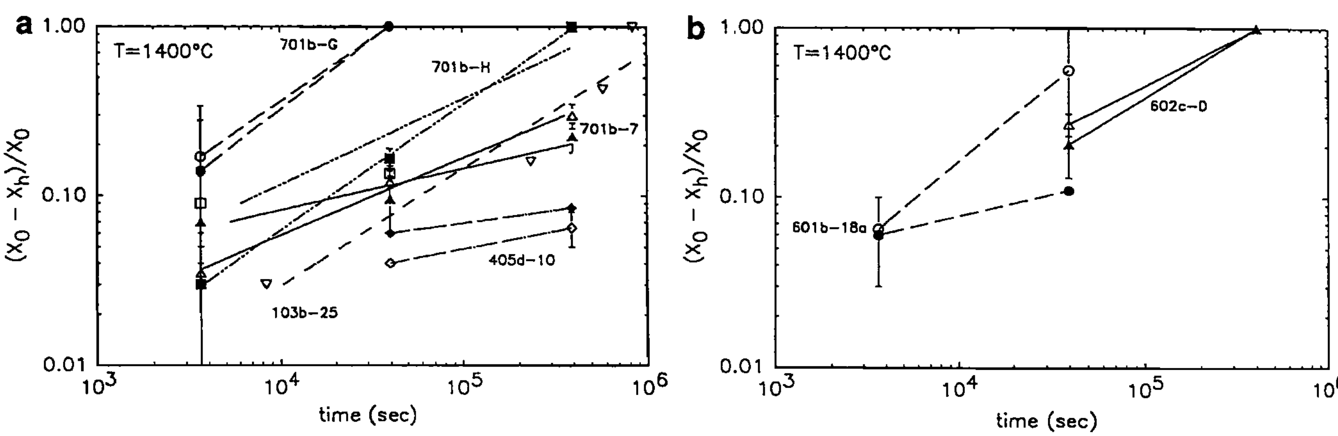

Fig. 9. Normalized crack length versus time for (a) (010) cracks measured in the <100> (open symbols) and <001> (filled symbols) directions and (b) (100) cracks measured in the <010> (open symbols) and <001> (filled symbols) directions experimentally healed at 1400°C (Table 5).

effects, we have simply taken the room condition values in our computation.

In long term experiments, as well as in nature, stress corrosion may be important. In minerals such as quartz and calcite, stable cracking can initiate at low velocities at a value of K_I somewhat less than K_{Ic}. This process of "subcritical crack growth" can result in inelastic stretching of the fluid inclusion before the onset of dynamic crack propagation or decrepitation. This effect is probably negligible in the type of experiments we discuss here. In tectonic settings, a lower limit to subcritical crack growth rate may be set by the kinetics of crack healing [*Atkinson*, 1984; *Smith and Evans*, 1984].

Healing Kinetics

Kirby and Green [1980] observed naturally decrepitated and subsequently healed fluid inclusions in San Carlos olivine and presented clear evidence that some plastic flow, i.e. stretching, accompanied uplift of the xenoliths. Previous experiments in San Carlos olivine, done in a buffering gas mixture at $fO_2 \leq 10^{-8}$ bars (0.001 Pa) indicate that the ratio of the spacing between spheres to the radius of the parent cylinder is about 7.8±1.9, indicating that the transport mechanism was either surface diffusion or, less likely, diffusion through the pore fluid itself [*Wanamaker and Evans*, 1985]. The time necessary for ovula-

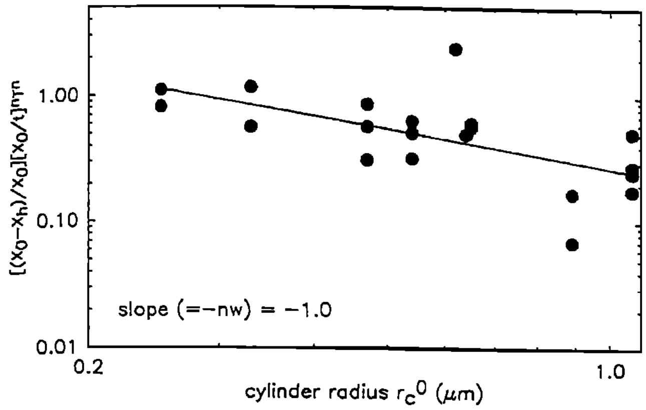

Fig. 10. Normalized crack length versus cylinder radius (Table 5) for cracks experimentally healed at 1400°C. The slope of the least squares fit to the data is equal to $-nw$.

tion (τ) was consistent with a relation, $\tau \propto r_c^4$, as would be predicted by the analytical treatment of the surface diffusion problem. The systematic differences in L/r_c and in the time for ovulation with changing buffering gases imply that the mechanism or kinetics of transport are being affected. If surface and lattice diffusion were influenced by oxygen fugacity in dissimilar ways, a changeover in transport mechanisms might result.

There are, however, two additional chemical complications. First, because the mechanical supports for the crystals were made of platinum, a reaction between olivine and platinum did occur in a small region around the points of contact, and involved the growth of pyroxene crystals and the formation of precipitates of FePt alloys. In addition, fine droplets of magnesio-alumino-silicate melts also were identified on the surface of the samples by EDS analysis. Both reactions were confined to the surface of the sample; in addition, we attempted to minimize the contact area. Thus we suppose, but do not know certainly, that the effect on the cracks located in the interior of the sample was small. It is possible that the reaction between platinum and the olivine has affected the rate of diffusion and thus the rate of crack healing measured in these experiments.

A second reaction also occurred which did involve the fluid inclusions. Laser Raman spectroscopy revealed that the CO_2 inclusions were reduced to form CO/CO_2 mixtures [*Pasteris and Wanamaker*, 1988] in equilibrium with the buffering gas mixtures used to maintain the stability field of olivine [*Nitsan*, 1974]. The reaction, which became evident after heat treatments of only 5 minutes at 1400°C, apparently involves the oxidation of the solid immediately surrounding the inclusions to form nonstoichiometric olivine or perhaps a second phase with concomitant reduction of the CO_2 to CO. It is possible that the variation of healing rate with oxygen fugacity results from changes in the kinetics of this oxidation-reduction reaction.

The healing models as formulated involve the assumption that the rate-limiting step is ovulation of the spherical pore from the cylindrical tube, as well as some untested assumptions regarding the geometry and rate of formation of cylinders [*see Hickman and Evans*, 1987]. Strictly speaking the regression distance derived is the distance from the original position of the crack to the latest spherical pore formed. In these experiments, we measured the distance to the innermost cylinder rather than the innermost spherical pores, because this distance was much larger and could be measured with more accuracy, and because the greatest change in physical properties probably occurs during this stage. More detailed data are necessary to test rigorously the form of the functional relationship between t and X_0-X_h; however, if eq. (15) is assumed to hold, the average exponent, n is 0.6±0.3. It is interesting to note that this value is quite similar to that obtained during experiments on cracks in calcite at 780°C [*Hickman and Evans*, 1987] and in alumina [*Evans and Charles*, 1977]. The latter experiments were done on polycrystalline material and have considerable added complexity owing to the complicated geometry and the presence of varying grain orientation. At present, the significance of the agreement between these largely phenomenological observations is not clear. Until more detailed theories and experimental data are available, the power law equation provides a useful working model to estimate crack healing kinetics.

Although there is considerable scatter in the healing data, it is clear that healing is accelerated by increasing temperature. Some observations of the kinetics of ovulation in San Carlos olivine were reported previously by *Wanamaker and Evans* [1985], who reported an activation energy for that process of 53±22 kcal/mol (222±88 kJ/mole). However, because of a zero-point calibration error, the temperature of those experiments was incorrectly reported as 1250°C instead of 1280°C; the activation energy for ovulation should then be corrected to 70±25 kcal/mole (293±100 kJ/mole). Using eq. (15) without correcting for differences in crack width, we calculate an apparent activation energy for crack healing $nQ/R \approx 29(\pm 18)\times 10^3$ K. If $n = 0.6$, then Q=96±60 kcal/mol (402±240 kJ/mole). However, because of the complex chemical changes occurring, and because it is difficult to verify all the assumptions inherent in the healing model, this value can only be regarded as an order of magnitude estimate.

Uplift and Alteration of Inclusions in San Carlos Olivine

In Figure 4c, we categorized the naturally decrepitated samples into two groups according to whether they were completely healed or partially healed. The theoretical calculations using the fracture mechanics model indicate that many of the completely healed specimens were decrepitated under a relatively high lithostatic pressure of the order of 1 GPa. This value is comparable to the pressure expected for the source region [*Frey and Prinz*, 1978] and would imply that these cracks formed soon after their entrainment in the ascending magma, consistent with their fully healed condition. The remainder of the partially healed cracks are distributed over the calculated pressure range from 1 GPa to 0 MPa. The cracks experimentally decrepitated at 0.1 MPa are generally consistent with the theoretical zero confining pressure limit. The location of the theoretically calculated isobars will be different for ratios of a/R other than that used in generating Figure 4c. The occasional discrepancies between the data and the theoretical calculations may indicate that there is a range of a/R for the fluid inclusions in the olivine xenoliths.

In Figure 11, we have used the naturally decrepitated and healed cracks to estimate the ascent rate of the olivine xenoliths from San Carlos. The lithostatic pressure at the time of decrepitation for a particular crack is estimated from the theoretical calculations in Figure 4c. Using equation 15, the experimentally measured crack healing rates at 1280 and 1400°C can be fit to the equation

$$[(X_0-X_h)/X_0][X_0/t]^n T^n = e^{\frac{nQ}{R}\left[\left[\frac{1}{1553}-\frac{1}{T}\right]-2.08\right]} \qquad (16)$$

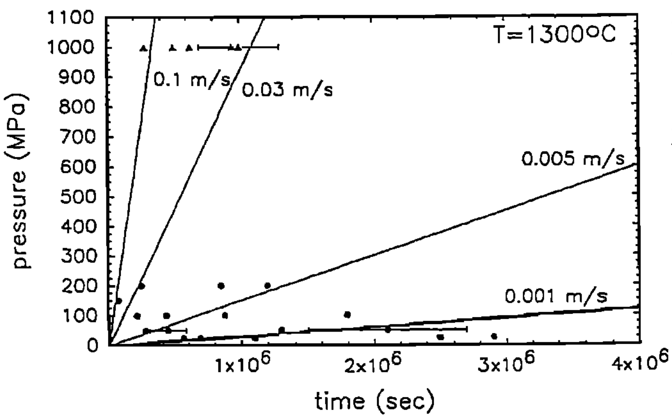

Fig. 11. Calculated ascent rates for naturally healed cracks in San Carlos xenoliths assuming a temperature of 1300°C. Data are plotted as decrepitation pressure versus crack healing time. Symbols are the same as in Fig. 4c. Representative error bars due to experimental uncertainty in the thermal activation energy for crack healing are shown.

where nQ/R=29(±18)x10^3 K, n=0.6, T is in K, X_0 and X_k are in µm, and t is in seconds. The time elapsed since decrepitation is calculated by substituting the measured value of $(X_0-X_k)/X_0$ and X_0 from Table 1 and the appropriate tenmperature for the ascending xenolith into eq. (16) and solving for t. We have assumed a crack healing temperature of 1300°C in the ascending magma plume and that healing is arrested once the xenolith has reached the surface.

The ascent rates calculated from the partially healed cracks range from 0.001 to 0.1 m/s. Alkali basalt ascent rates are estimated to be between 0.01 and 5 m/s [*Spera*, 1984]. Rates calculated from the completely healed cracks tend to be faster because healing was probably completed before eruption at the surface. Slower ascent rates could be due to ponding of magma at depth before eruption at the surface or continued crack healing after eruption. If the temperature of the ascending magma is higher than 1300°C, the calculated ascent rates would be correspondingly faster, whereas a lower temperature would result in slower calculated ascent rates.

Not all of the fluid inclusions in the San Carlos olvine xenoliths decrepitated during ascent. Whether or not a particular fluid inclusion will decrepitate depends on the pressure/temperature history of the xenolith and the fluid density and geometry of the inclusion. *Wanamaker and Evans* [1989] investigated the plastic deformation of fluid inclusions in the same xenoliths and noted that even those inclusions which decrepitated exhibited dislocation structures indicating that they had stretched before cracking. Several different scenarios can be hypothesized for the entrainment of these xenoliths into the ascending magma. Entrainment may be isothermal but ascent rate, and therefore P_f-P_c, may increase with decreasing depth. Alternatively, the magma may be hotter than the surrounding mantle and entrainment may be accompanied by an increase in temperature and thus P_f-P_c. Both of these scenarios may promote initial plastic deformation of the inclusions followed by brittle fracture. Differences in the mode of deformation among inclusions in the same xenolith indicate a distribution in (1) fluid densities, as a result of entrapment under changing pressure/temperature conditions, or (2) the ratio of a/R.

Microcracks are commonly observed in crustal rocks as well. Their origin is often attributed to microfracturing by internal stresses induced by mismatches in thermoelastic moduli on a grain to grain scale [e.g. *Nur and Simmons*, 1970]. However, fluid inclusion decrepitation can also contribute to microcracking during the unroofing process. The fracture mechanics model presented here is a first attempt to quantify this process. Of course, stress intensity factors and crack healing kinetics appropriate for minerals found in crustal rocks must be included.

CONCLUSIONS

A fracture mechanics model has been developed to describe the initiation, propagation, and arrest of fluid inclusion decrepitation in San Carlos olivine. Correlations between fluid inclusion size and both decrepitation pressure and crack extension have been investigated by incorporating the presence of flaws associated with the fluid inclusions into the fracture mechanics model. These flaws are modelled as annular cracks radiating from the fluid inclusion surface. Data from the experimental decrepitation of fluid inclusions in olivine suggest that the ratio of the flaw length a to the inclusion radius R is between 0.1 and 0.3, corresponding to an initial crack length on the order of 1 µm.

The fracture mechanics model can be used to derive an implicit equation relating the initial flaw length to the final crack length as a function of inclusion radius and confining pressure. The experimental results on crack extension are again bracketed by $0.1<a/R<0.3$.

After decrepitation, the cracks were experimentally healed at 1280 and 1400°C. Healing occurs due to transport of material in response to gradients in chemical potential along the crack surface. During healing, the open crack porosity is modified first into cylindrical pores and then spherical pores. Healing rates are controlled by the geometry of the crack and an Arrhenius term containing the activation energy for diffusion.

Cracks on the order of 2-30x10^3 µm^2 and approximately 1 µm wide are completely healed within 10-100 hours at 1400°C. The experimentally determined value of the geometric parameter n is 0.6, and the apparent activation energy nQ/R is 29(±18)x 10^3 K.

The naturally decrepitated and healed fluid inclusions in San Carlos olivine can be used to estimate the ascent rate of the xenoliths. The fracture mechanics model allows the lithostatic pressure at decrepitation to be calculated while the crack healing kinetics provide an estimate of the time elapsed since decrepitation. Assuming that the temperature during ascent was 1300°C, the range of healed crack morphologies in San Carlos olivine suggest ascent rates between 0.001 and 0.1 m/s, consistent with those estimated using other techniques for other alkali basalt magmas [*Spera*, 1984]. Lower or higher temperatures would result in relatively slower or faster calculated ascent rates, respectively.

APPENDIX

We describe here the detailed derivation of the results of the fracture mechanics model. We are interested in the evaluation of the stress intensity factor at the tip of an annular crack at a spherical void. The fluid inclusion and crack surfaces are both subjected to a fluid pressure P_f and the solid is subjected to a remote confining pressure P_c (Figure A1).

Since the solid is assumed to be homogeneous and linearly elastic, this problem can be treated as the superposition of the two configurations shown in Figure A2. It can be seen that the

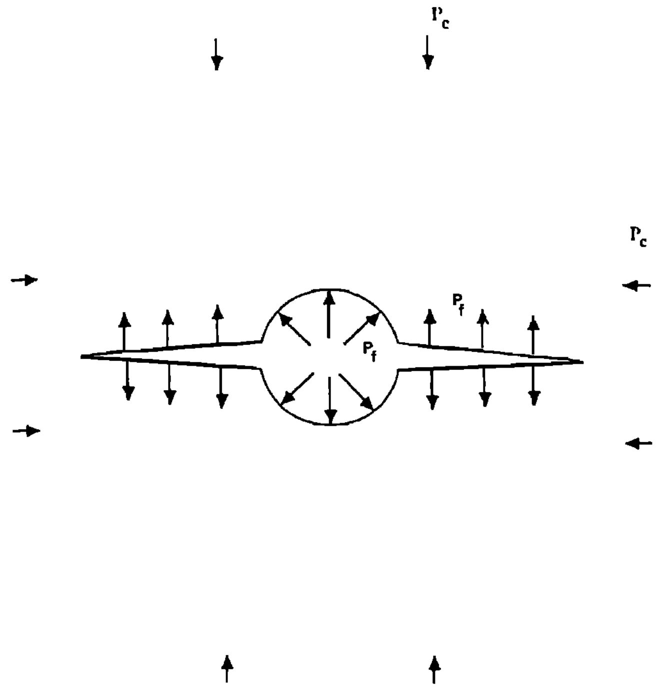

Fig. A1. The stresses acting on an annular crack at a spherical void. The remote stress field is a hydrostatic pressure given by P_c, and the fluid pore pressure is P_f.

lefthand configuration with homogeneous loading due to hydrostatic pressure does not contribute to any stress singularities at the crack tip. Hence, one only needs to consider the righthand configuration (corresponding to a remotely applied hydrostatic tension P_f - P_c on the solid) in calculating the stress intensity factor.

The analogous problem of uniaxial tension loading has been investigated extensively in the materials science literature [e.g. *Evans et al.*, 1979; *Green*, 1980]. If the dimension of the crack (X) is greater than the void radius, then the stress intensity factor K_1 can be evaluated conveniently using a Green's function technique. Specifically, if the axis of symmetry of the annular crack is taken to be the z-axis with the crack tip located at r=X, and if the tensile stress acting normal to the annular plane in the absence of the crack has been determined to be $\sigma_{zz}(r,0)$, then the stress intensity factor K_1 at the tip r=X may be evaluated by the following integral:

$$K_1 = \frac{2}{\sqrt{(\pi c)}} \int_X^c \frac{r\,\sigma_{zz}(r,0)\,dr}{\sqrt{(c^2-r^2)}} \tag{A1}$$

with $c = X+R$. The use of this integral is motivated by the observation that the stress intensity factor due to the application of a ring of point forces at r on the surface of a penny-shaped crack of radius c in an infinite medium is given by $(2/\sqrt{(\pi c)})(r/\sqrt{(c^2-r^2)})$ [*Barenblatt*, 1962]. Equation (A1) therefore represents the superposition of this Green's function.

For a spherical void under remote hydrostatic tension, the stress component of interest is given by:

$$\sigma_{zz}(r,0) = (P_f-P_c)\left[1+\frac{1}{2}\left[\frac{R}{r}\right]^3\right] \tag{A2}$$

On substituting (A2) into (A1), we arrive at equation (7) given in the main text.

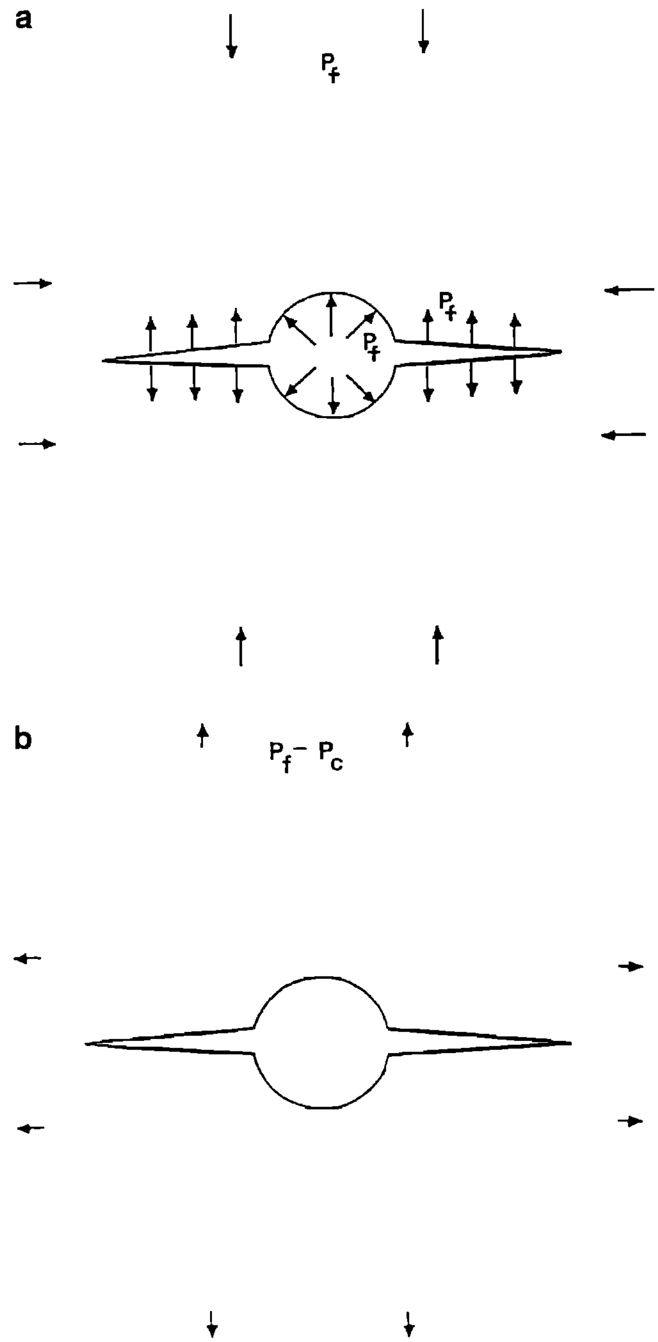

Fig. A2. By linear superposition, the boundary value problem shown in Figure A1 can be considered separately as: (a) a homogeneous hydrostatic loading with confining pressure and fluid pore pressure both equal to P_f, and (b) a remote hydrostatic tension P_f-P_c acting on an annular crack at a spherical void, both of which are stress free. The stress field for the first configuration does not have any singularity at the crack tip, hence, only the seconc configuration needs to be considered to evaluate the stress intensity factor.

Strictly speaking, the above approach applies to an annular crack with no tensile opening for $r \leq R$. In the spherical void problem, appreciable opening occurs at the interface between the spherical surface and the crack surface (i.e. r=R). Comparison with numerical computation has shown that the contribution of this opening to K_1 is negligible for crack length X longer than the void radius R [*Green*, 1980]. Our olivine data for crack arrest of both experimentally and naturally decrepitated samples show that the final crack lengths X_0 are at least three times the corresponding inclusion radii. Hence the above solution can be used for the crack arrest phase.

On the other hand, the initial crack length a is sufficiently short at the onset of decrepitation that the solution obtained by the Green's function technique underestimates the stress intensity factor. However, an exact assymptotic solution can be obtained for the case a/R approaching zero. In this case, the curvature of the spherical surface can be neglected and the crack tip stress field approaches that for an edge crack of length a in a semi-infinite medium, which is well known to be the local stress multiplied by a factor $1.1215\sqrt{(\pi a)}$. It can be seen from equation (A2) that the local stress at $r=R$ is $1.5(P_f-P_c)$, hence the stress intensity factor is given by $1.68(P_f-P_c)\sqrt{(\pi a)}$ (equation (3)).

In our problem, the initial crack dimension is intermediate between the cases of a/R<<1 and a/R>1. Hence, neither the asymptotic solution nor the Green's function solution applies. A similar problem is encountered in analyzing cracking at spherical voids in ceramic materials [*Evans et al.*, 1979] for which the a/R ratio typically falls in the range between 0 and 1. We have opted to use the asymptotic solution which provides a lower bound on the decrepitation pressure.

Ad hoc schemes have been developed in the materials science literature to calculate the stress intensity factor by interpolation between the two solutions shown in Figure 4a. We have tried one such interpolation scheme proposed by *Green* [1980]. As expected, the interpolation solution gives a higher decrepitation pressure. It also predicts an amount of crack extension which is somewhat greater than what is shown in Figure 4. Considering the various uncertainties in the model in connection with the equation of state of the fluid filling the cracks, the physical parameters, and fluid inclusion geometry, we believe that this type of refinement in the analysis is probably of secondary importance. Hence, the tedious algebra involved for this interpolation technique is not included in this paper.

Acknowledgments. We would like to thank L. S. Hollister of Princeton University and T. L. Grove of M. I. T. for help with microthermometry and experimental petrology. This work was supported by grants from NSF (EAR-8708598) to Evans and (EAR-8512407) to Wong and USGS (14-08-001-G1340, Evans; -G1352, Wong). Support from the Office of Basic Energy Sciences of the U. S. Department of Energy during the preparation of this paper is gratefully acknowledged.

REFERENCES

Atkinson, B. K., Subcritical crack growth in geological materials, *J. Geophys. Res.*, *89*, 4077-4114, 1984.

Barenblatt, G., Mathematical theory of equilibrium cracks in brittle fracture, *Adv. Appl. Mech.*, *7*, 55-129, 1962.

Binns, P. R., and R. J. Bodnar, Decrepitation behavior of fluid inclusions in quartz at one atmosphere confining pressure, *Eos Trans. AGU*, *67*, 399, 1986.

Bodnar, R. J., and P. M. Bethke, Systematics of stretching of fluid inclusions I: fluorite and sphalerite at 1 atmosphere confining pressure, *Econ. Geol.*, *79*, 141-161, 1984.

Bodnar, R. J., P. R. Binns, and D. L. Hall, Synthetic fluid inclusions-VI. Quantitative evaluation of the decrepitatiion behaviour of fluid inclusions in quartz at one atmosphere confining pressure, *J. Metamorph. Geol.*, *7*, 229-242, 1989.

Brace, W. F., Permeability from resistivity and pore shape, *J. Geophys. Res.*, *82*, 3343-3349, 1977.

Brace, W. F. and J. B. Walsh, Some direct measurements of the surface energy of quartz and orthoclase, *Am. Mineral.*, *47*, 1111-1122, 1962.

Evans, A. G. and E. A. Charles, Strength recovery by diffusive crack healing, *Acta Metall.*, *25*, 919-927, 1977.

Evans, A. G., D. R. Biswas, and R. M. Fulrath, Some effects of cavities on the fracture of ceramics: I, cylindrical cavities; II, spherical cavities, *J. Am. Ceram. Soc.*, *62*, 95-106, 1979.

Fredrich, J. T., and T. -f. Wong, Micromechanics of thermally induced cracking in three crustal rocks , *J. Geophys. Res.*, *91*, 12743-12764, 1986.

Frey, F. A. and M. Prinz, Ultramafic inclusions from San Carlos, Arizona: petrologic and geochemical data bearing on their petrogenesis, *Earth Planet. Sci. Lett.*, *38*, 129-176, 1978.

Gilman, J. J., Direct measurements of the surface energies of crystals, *J. Appl. Phys.*, *31*, 2208-2218, 1960.

Green, D. J., Stress intensity factor estimaters for annular cracks at spherical voids, *J. Am. Ceram. Soc.*, *63*, 342-344, 1980.

Green, H. W. and S. V. Radcliffe, Fluid precipitates in rocks from the earth's mantle, *Geol. Soc. Am. Bull.*, *86*, 846-852, 1975.

Hall, D. L. and R. J. Bodnar, Comparison of fluid inclusion decrepitation and acoustic emission profiles of Westerly granite and Sioux quartzite, *Tectonophysics*, *168*, 1989.

Hickman, S. H. and B. Evans, Influence of geometry upon crack healing rate in calcite, *Phys. Chem. Miner.*, *15*, 91-102, 1987.

Hollister, L. S. and M. L. Crawford (editors), *Short Course in Fluid Inclusions: Applications to Petrology*, *6*, Mineralogical Association of Canada, Calgary, 304 pp., 1981.

Kirby, S. H. and H. W. Green, Dunite xenoliths from Hualalai volcano: evidence for mantle diapiric flow beneath the island of Hawaii, *Am. J. Sci.*, *280-A*, 550-575, 1980.

Kumazawa, M., and O. L. Anderson, Elastic moduli, pressure derivatives and temperature derivatives of single crystal olivine and single crystal forsterite, *J. Geophys. Res.*, *74*, 5961-5972, 1969.

Larson, L. T., J. D. Miller, J. E. Nadeau, and E. Roedder, Two sources of error in low temperature inclusion homogenization determination, and corrections on published temperatures for the East Tennessee and Laisvall deposits, *Econ. Geol.* , *68*, 113-116, 1973.

Lawler, J. P., and M. L. Crawford, Stretching of fluid inclusions resulting from a low- temperature micro thermometric technique, *Econ. Geol.*, *78*, 527-529, 1983.

Lawn, B. R., and T. R. Wilshaw, *Fracture of Brittle Solids*, Cambridge University Press, New York, 204 pp, 1975.

Murck, B. W., R. C. Burruss, and L. S. Hollister, Phase equilibria in fluid inclusions in ultramafic xenoliths, *Am. Mineral.*, *63*, 40-46, 1978.

Nicholls, F. A., On the spheroidization of rod-shaped particles of finite length, *J. Mater. Sci.*, *11*, 1077-1082, 1976.

Nicholls, F. A. and W. W. Mullins, Morphological changes in a surface of revolution due to a capillarity-induced surface diffusion, *J. Appl. Phys.*, *36*, 1826-1835, 1965a.

Nicholls, F. A. and W. W. Mullins, Surface(interface) and volume diffusion contributions to morphological changes driven by capillarity, *Trans. Am. Inst. Min. Metall. Pet. Eng.*, *233*, 1940-1948, 1965b.

Nitsan, U., Stability field of olivine with respect to oxidation and reduction, *J. Geophys. Res.*, *79*, 706-711, 1974.

Nur, A., and G. Simmons, The origin of small cracks in igneous rocks, *Int. J. Rock Mech. Min. Sci.*, *7*, 307-314, 1970.

Ohnaka, M., The quantitiative effect of hydrostatic confining pressure on the compressive strength of crystalline rocks, *J. Phys. Earth*, *21*, 285-303, 1973.

Pasteris, J. D. and B. J. Wanamaker, Laser Raman microprobe analysis of experimentally re-equilibrated fluid inclusions in olivine: some implications for mantle fluids, *Am. Mineral.*, *73*, 1074-1088, 1988.

Poland, E. L., Stretching of fluid inclusions at confining pressure up to 1 kilobar, M. S. thesis, 90pp., Univ. of Calif., Berkeley, 1982.

Roedder, E., Liquid CO_2 inclusions in olivine-bearing nodules and phenocrysts from basalts, *Am. Mineral.*, *50*, 1746-1782, 1965.

Roedder, E., *Fluid Inclusions*, *Rev. Mineral.*, *12*, Mineralogical Society of America, Washington, D. C., 644pp., 1984.

Rummel, F, and R. B. Winter, Fracture mechanics as applied to hydraulic fracturing stress measurements, *Earthquake Predict. Res.*, *2*, 33-45, 1983.

Sammis, C. G. and B. R. Julian, Fracture instabilities accompanying dike intrusion, *J. Geophys. Res.*, *92*, 2597-2605, 1987.

Shankland, T. J., R. J. O'Connell, and H. S. Waff, Geophysical constraints on partial melt in the upper mantle, *Rev. Geophys.*, *19*, 394-406, 1981.

Simmons, G. and D. Richter, Microcracks in rocks, *The Physics and*

Chemistry of Minerals and Rocks, edited by R. G. J. Strens, pp. 105-137, John Wiley, New York, 1976.

Simmons, G., and H. Wang, *Single Crystal Elastic Constants and Calculated Aggregate Properties*, M.I.T. Press, 1971.

Smith, D. L. and B. Evans, Diffusional crack healing in quartz, *J. Geophys. Res*, *89*, 4125-4135, 1984.

Spera, F. J., Carbon dioxide in petrogenesis III: role of volatiles in the ascent of alkaline magma with special reference to xenolith-bearing mafic lavas, *Contrib. Mineral. Petrol.*, *88*, 217-232, 1984.

Sprunt, E. S. and A. Nur, Microcracking and healing in granites: new evidence from cathodoluminescence, *Science*, *205*, 495-497, 1979.

Swain, M. V., and B. K. Atkinson, Fracture surface energy of olivine, *Pure Appl. Geophys.*, *116*, 866-872, 1978.

Timoshenko, S., and J. N. Goodier, *Theory of Elasticity*, McGraw-Hill, New York, 1951.

Tugarinov, A. I., and V. B. Naumov, Dependence of the decrepitation temperature of minerals on the composition of their gas-liquid inclusions and hardness, *Dokl. Akad. Nauk SSSR*, *195*, 112-114, 1970.

Ulrich, M. R. and R. J. Bodnar, Systematics of stretching of fluid inclusions II: Barite at 1 atm confining pressure, *Econ. Geol.*, *83*, 1037-1046, 1988.

Vukalovich, M. P. and V. V. Altunin, *Thermophysical Properties of* CO_2, Collets, London, 389pp., 1969.

Walsh, J. B., The effect of cracks on the compressibility of rocks, *J. Geophys. Res.*, *70*, 381-389, 1965.

Wanamaker, B. J., and B. Evans, Mechanical re-equilibration of fluid inclusions in San Carlos olivine by power law creep, *Contrib. Mineral. Petrol.*, *102*, 102-111, 1989.

Wanamaker, B. J., and B. Evans, Diffusional crack healing in olivine, in *Point Defects in Minerals, Geophys. Monogr. Ser.*, vol. 31, edited by R. N. Schock, pp. 194-210, AGU, Washington, D. C., 1985.

B. Evans, Department of Earth, Atmospheric, and Planetary Sciences, Massachusetts Institute of Technology, Cambridge, MA 02139.

B. J. Wanamaker, L-201, Lawrence Livermore National Laboratory, P. O. Box 808, Livermore, CA 94550.

T.-f. Wong, Department of Earth and Space Sciences, State University of New York at Stony Brook, Stony Brook, NY 11794.

(Received June 30, 1989;
revised January 29, 1990;
accepted February 16, 1990.)